Viscous adhesion of vibrating sheets: elastohydrodynamic with inertia and compressibility effects

Stéphane Poulain[1]†, Timo Koch[1,2], L. Mahadevan[3,4] and Andreas Carlson[1,5]‡

[1]Mechanics Division, Department of Mathematics, University of Oslo, 0316 Oslo, Norway

[2]Department of Scientific Computing and Numerical Analysis, Simula Research Laboratory, 0164 Oslo, Norway

[3]Paulson School of Engineering and Applied Sciences, Harvard University, Cambridge, MA 02138, USA

[4] Department of Physics and Department of Organismic and Evolutionary Biology, Harvard University, Cambridge, MA 02138, USA

[5] Department of Medical Biochemistry and Biophysics, Umeå University, 901 87, Umeå, Sweden

(Received xx; revised xx; accepted xx)

Inspired by recent experiments demonstrating that vibrating elastic sheets can function as seemingly contactless suction cups, we investigate the elastohydrodynamic hovering of a thin elastic sheet vibrating near a rigid substrate. Previous theoretical work suggests that the hovering height results from a balance between the active forcing that triggers the vibrations, the bending stresses associated with the sheet's deformation, the viscous lubrication flow between the sheet and the substrate, and the sheet's weight. Here, we extend this analysis beyond the asymptotic regime of weak forcing and explore the regime of strong forcing through numerical simulations. We identify the scalings for the equilibrium hovering height and the maximum load that can be supported. We further quantify the influence of fluid inertia and compressibility. Both effects are found to introduce repulsive contributions to the net force on the sheet, which can significantly reduce its adhesive strength. Beyond providing insights into soft contactless grippers and swimming near surfaces, our analysis is relevant to the elastohydrodynamics of squeeze films and near-field acoustic levitation.

Key words: Fluid-structure interactions, Lubrication theory, Gas dynamics

† Email address for correspondence: stephapo@uio.no
‡ Email address for correspondence: acarlson@uio.no

1. Introduction

Contactless gripping or hovering near surfaces is desirable in many applications (Vandaele *et al.* 2005). Fluid-mediated strategies include acoustic levitation to manipulate small objects (Andrade *et al.* 2018), Bernoulli grippers to grab delicate items (Waltham *et al.* 2003; Li *et al.* 2015), hovercrafts travelling on air cushions, and ground-effect flight used by both birds and vehicles (Rayner 1991; Ollila 1980). In parallel, soft robotics (Whitesides 2018) has emerged as an alternative to traditional mechanical systems with applications in handling fragile objects (Shintake *et al.* 2018) and bio-inspired locomotion (Calisti *et al.* 2017). Combining contactless dynamics with soft designs, Argentina *et al.* (2007) theoretically proposed that an elastic sheet sustaining travelling waves and placed next to a surface could levitate and translate owing to elastohydrodynamic interactions. More recently, Colasante (2015) and Weston-Dawkes *et al.* (2021) devised a novel strategy: they showed experimentally that attaching a vibration motor to an elastic sheet creates a seemingly contactless suction cup that can adhere to surfaces or pick up objects weighing up to several kilograms (see Colasante (2016) and references in Ramanarayanan & Sánchez (2024)), offering a possible alternative to state-of-the-art contactless grippers. In a broader context, recent studies have highlighted the roles of elastohydrodynamic and vibrations in adhesion: viscous effects have been shown to influence bonding fronts (Rieutord *et al.* 2005; Poulain *et al.* 2022), the viscous Stefan adhesion mechanism has been analysed for deformable surfaces (Shao *et al.* 2023; Bertin *et al.* 2025), and vibrations have been found to enhance dry adhesion (Shui *et al.* 2020; Tricarico *et al.* 2025) and to improve the stability of suction cups (Zhu *et al.* 2006; Wu *et al.* 2023).

In our earlier publication (Poulain *et al.* 2025), we modelled the viscous flow in the thin gap between a wall and an actuated elastic sheet. We demonstrated how a time-reversible forcing of the soft sheet triggers a non-reversible response, an effect previously examined in the context of microorganism swimming with flagella (Wiggins & Goldstein 1998; Wiggins *et al.* 1998; Yu *et al.* 2006; Lauga 2007). Indeed, elastohydrodynamic interactions enable breaking the time-reversal symmetry of viscous flows and circumventing the scallop theorem (Taylor 1967; Purcell 1977; Bureau *et al.* 2023; Rallabandi 2024), generating a net effect that attracts or repels the sheet depending on the spatial profile of the forcing. For a localised central forcing, we showed that the elastohydrodynamic effects attract the sheet towards the surface against gravity, enabling adhesion and hovering. This viscous elastohydrodynamic mechanism rationalises qualitatively the experiments of Colasante (2016) and Weston-Dawkes *et al.* (2021). While our analysis isolated the essential physics, it relied on asymptotic calculations assuming a weak forcing and on the assumptions of incompressible and inertialess flow, leveraging lubrication theory. A more comprehensive understanding, however, may require considering the inertia and compressibility of the fluid, as highlighted by Ramanarayanan *et al.* (2022); Ramanarayanan & Sánchez (2022, 2024).

Corrections to lubrication theory have long been studied, particularly in squeeze-film settings relevant to bearings (Moore 1965) and resonant micro-electro-mechanical systems (MEMS) (Bao & Yang 2007; Pratap & Roychowdhury 2014; Fedder *et al.* 2015). In standard squeeze films, two surfaces of length $\tilde{R}$ immersed in a fluid with ambient pressure $\tilde{p}_a$, ambient density $\tilde{\rho}_a$ and dynamic viscosity $\tilde{\mu}$ oscillate with the distance separating them evolving harmonically as $\tilde{h}(\tilde{t}) = \tilde{h}_0\left(1 + a\sin(\tilde{\omega}\tilde{t})\right)$, where $0 < a < 1$. Experimental observations reveal that

the flow in the gap can generate net normal forces or damping effects that are not predicted by classical lubrication theory, which only considers viscous effects.

Considering the viscous and compressible flow of an ideal gas, Taylor & Saffman (1957) and Langlois (1962) showed that a repulsive normal force between the two surfaces arises for finite Squeeze number $\mathrm{Sq} = \tilde{\mu}\tilde{\omega}\tilde{R}^2/\tilde{h}_0^2\tilde{p}_a > 0$, i.e., when the magnitude of viscous stresses is comparable to the ambient pressure. These effects, studied in more detail since (Bao & Yang 2007; Melikhov *et al.* 2016; Ramanarayanan *et al.* 2022), allow for the squeeze film levitation of small objects (Shi *et al.* 2019), are relevant to MEMS sensors such as atomic force microscopes employing vibrating micro-cantilever plates or beams (Bao & Yang 2007; Wei *et al.* 2021), and may have applications in the design of haptic surfaces (Wiertlewski *et al.* 2016). More generally, squeeze films belong to an interesting class of elastohydrodynamic problems where compressible effects are significant even at low Mach numbers (e.g., Mandre *et al.* (2009); Peng *et al.* (2023)). Compressible squeeze flows can also be coupled with elastic deformations: instead of using rigid-body vibrations, leveraging flexural vibrations has been proposed to enhance levitation efficiency (Hashimoto *et al.* 1996; Minikes & Bucher 2003) and allow lateral translation of the levitated object (Ueha *et al.* 2000; Andrade *et al.* 2018). The coupling between the elastic deformations of thin cantilever plates with squeeze flows is also key for MEMS (Lee *et al.* 2009; Pandey & Pratap 2007).

Fluid inertia can also contribute to squeeze film dynamics, and inertial corrections to lubrication theory have been derived for finite Reynolds number $\mathrm{Re} = \tilde{\rho}_a\tilde{\omega}\tilde{h}_0^2/\tilde{\mu} > 0$ in the context of bearings (Ishizawa 1966; Kuzma 1968; Tichy & Winer 1970; Jones & Wilson 1975) and later applied to squeeze film levitation (Atalla *et al.* 2023; Liu *et al.* 2023) and MEMS (Veijola 2004). This corresponds to the regime where the forcing timescale $\tilde{\omega}^{-1}$ and the viscous diffusion timescale $\tilde{\rho}_a\tilde{h}_0^2/\tilde{\mu}$ are comparable. For incompressible flows, inertia leads to a repulsive normal force between the surfaces. The aforementioned analytical corrections to Reynolds' lubrication theory are limited to rigid geometries or specific types of deformation. Rojas *et al.* (2010) derived lubrication equations with inertial corrections, which naturally accommodate arbitrary deformable geometries. They have successfully applied this framework to free-surface phenomena; however, to our knowledge, it has not yet been extended to elastohydrodynamics and soft lubrication (Skotheim & Mahadevan 2005). More generally, flows at intermediate Reynolds numbers, where both viscous and inertial effects are significant, arise in a variety of physical systems. One of the most striking examples is steady streaming, the generation of a mean flow from periodic oscillations (Riley 2001). Streaming is strongly influenced by confinement, as studied in the context of atomic force microscopes and surface force apparatus (Fouxon & Leshansky 2018; Fouxon *et al.* 2020; Zhang *et al.* 2023; Bigan *et al.* 2024), and in physiological flows in tubes (Hall 1974; Dragon & Grotberg 1991). Interestingly, streaming can also occur when soft boundaries are involved, even in the absence of inertia (Bhosale *et al.* 2022; Cui *et al.* 2024; Pande *et al.* 2023; Zhang & Rallabandi 2024).

Returning to squeeze films, an object may experience a net attractive force towards a vibrating surface, rather than a repulsive force, an effect leading to so-called inverted near-field acoustic levitation (Takasaki *et al.* 2010; Andrade *et al.* 2020). This observation has recently been theoretically rationalized by Ramanarayanan *et al.* (2022), who found that, surprisingly, incorporating both inertial and compressible effects in the lubrication dynamics reveals the possibility of an attractive force when including second-order inertial effects. Ramanarayanan & Sánchez (2022, 2024) later

extended their analysis to deformable geometries, showing an enhancement of the attractive effect. In contrast, our previous work (Poulain *et al.* 2025) demonstrated that viscous, inertialess, and incompressible fluid-structure interactions alone can produce an adhesive effect when an elastic sheet is driven near a surface. In this regime relevant to the experiments of Colasante (2015) and Weston-Dawkes *et al.* (2021), we anticipate that inertial and compressible effects play a secondary role, entering as corrections rather than dictating the primary viscous adhesion mechanism. Indeed, inverted near-field acoustic levitation typically supports only objects weighing a few milligrams (Andrade *et al.* 2020), whereas the viscous mechanism we uncovered predicts a lift capacity on the order of kilograms under typical experimental conditions, in agreement with observations.

This article is organised as follows. In §2, we present the elastohydrodynamic framework to describe a vibrating elastic sheet lubricated by a thin fluid layer, together with the nondimensional form of the governing equations. Section 3 focuses on the viscous regime and introduces the distinction between the limits of weak and strong forcing. We provide the corresponding scaling laws for the equilibrium adhesion height and the maximum sheet's weight before adhesion failure. Sections 4 and 5 extend the analysis to include the first-order effects of fluid inertia and compressibility, characterised by finite Reynolds and Squeeze numbers, respectively. Numerical simulations show that both effects weaken adhesion strength compared with the purely viscous model, in agreement with asymptotic predictions in the rigid-sheet limit (appendices D and E). Finally, we summarize and discuss the findings in §6.

2. Problem setup and governing equations

2.1. *Problem setup*

We consider the system shown in figure 1: an elastic sheet of radius $\tilde{R}$, thickness $\tilde{e}$, density $\tilde{\rho}_s$, Poisson ratio ν, Young's modulus $\tilde{E}$, and bending modulus $\tilde{B} = \tilde{E}\tilde{e}^3/12(1-\nu^2)$, is placed near a solid substrate. The surrounding fluid is Newtonian with ambient density $\tilde{\rho}_a$, ambient pressure $\tilde{p}_a$, and a constant viscosity $\tilde{\mu}$. The sheet is forced at its centre by a harmonic active load with angular frequency $\tilde{\omega}$, radius $\tilde{\ell}$, and force magnitude $\tilde{F}_a$. In this setting, we aim to establish equilibrium conditions under which the elastic sheet hovers at a finite, stable time-averaged distance from the wall despite the gravitational pull.

An important characteristic scale of the system is the elastohydrodynamic height (Poulain *et al.* 2025)

$$\tilde{H}_{\mathrm{bv}} = \tilde{R}^2 \left(\frac{\tilde{\mu}\tilde{\omega}}{\tilde{B}} \right)^{1/3}, \tag{2.1a}$$

for which viscous stresses scaling as $\tilde{\mu}\tilde{\omega}\tilde{R}^2/\tilde{H}_{\mathrm{bv}}^2$ and bending stresses scaling as $\tilde{B}\tilde{H}_{\mathrm{bv}}/\tilde{R}^4$ balance. Associated with $\tilde{H}_{\mathrm{bv}}$ is the aspect ratio $\varepsilon_{\mathrm{bv}} = \tilde{H}_{\mathrm{bv}}/\tilde{R}$, and an elastohydrodynamic force scale

$$\tilde{F}_{\mathrm{bv}} = (\tilde{\mu}\tilde{\omega}\tilde{B}^2)^{1/3}. \tag{2.1b}$$

The scale for elastohydrodynamic stresses is then $\tilde{F}_{\mathrm{bv}}/\tilde{R}^2$. In the remainder of the article, we mostly work with dimensionless quantities (written throughout without

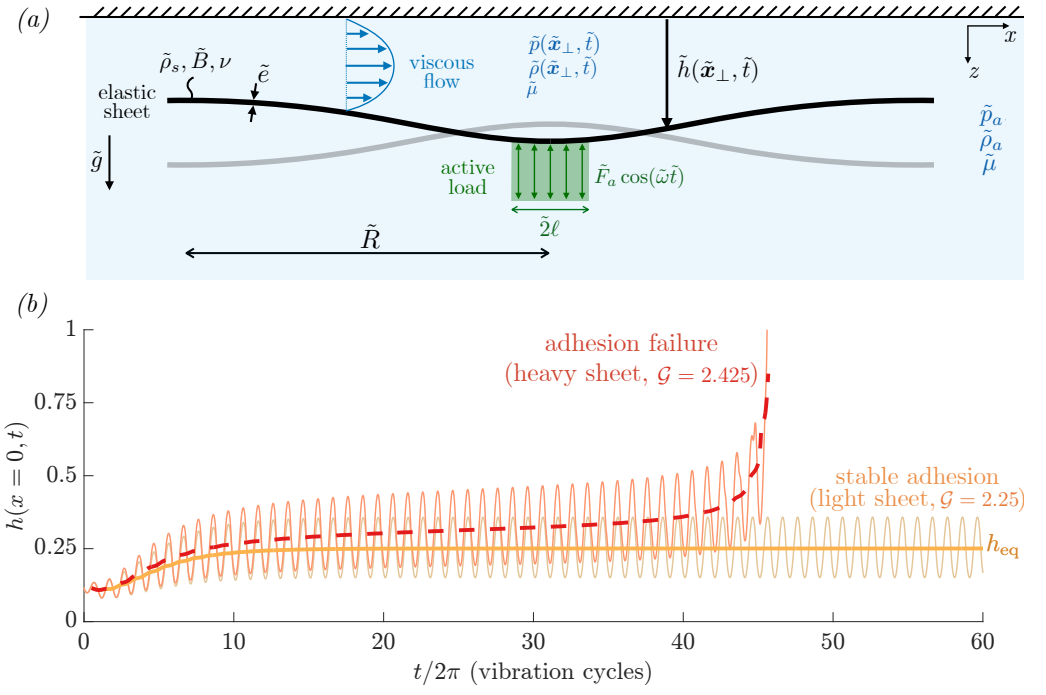

Figure 1: (*a*) An elastic sheet (radius $\tilde{R}$, density $\tilde{\rho}_s$, bending rigidity $\tilde{B}$, Poisson's ratio ν, thickness $\tilde{e}$) immersed in a fluid (ambient density $\tilde{\rho}_a$, ambient pressure $\tilde{p}_a$, dynamic viscosity $\tilde{\mu}$) and forced periodically at its centre (force $\tilde{F}_a$, angular frequency $\tilde{\omega}$, radius $\tilde{\ell}$) is placed below a solid substrate with gravity pointing downward. $\boldsymbol{x}_\perp = (x, y)$ represent the horizontal coordinates. The dynamics is characterized by dimensionless numbers defined in table 1: Reynolds number $\mathrm{Re}_{\rm bv}$, Squeeze number $\mathrm{Sq}_{\rm bv}$, solid inertia $\mathcal{I}_{\rm bv}$, weight $\mathcal{G}$, and forcing strength α. (*b*) When $\mathcal{G}$ is small enough, the sheet hovers around an equilibrium position $h_{\rm eq}$ (illustrated here for $\alpha = 5$, $\mathcal{G} = 2.25$ and a purely viscous dynamics, $\mathcal{I}_{\rm bv} = \mathrm{Re}_{\rm bv} = \mathrm{Sq}_{\rm bv} = 0$). Above a critical weight, the sheet cannot adhere to the substrate (shown for $\mathcal{G} = 2.425$). Thin lines represent the gap thickness at the centre of the sheet $h(x = 0, t)$ and thick lines the time-averaged $\langle h \rangle(x = 0, t)$.

a tilde, in contrast to dimensional quantities):

$$t = \tilde{t}\tilde{\omega}, \quad \boldsymbol{x}_\perp = \frac{\tilde{\boldsymbol{x}}_\perp}{\tilde{R}}, \quad h(\boldsymbol{x}_\perp, t) = \frac{\tilde{h}(\tilde{\boldsymbol{x}}_\perp, \tilde{t})}{\tilde{H}_{\rm bv}},$$
$$p(\boldsymbol{x}_\perp, t) = \frac{\tilde{p}(\tilde{\boldsymbol{x}}_\perp, \tilde{t})}{\tilde{F}_{\rm bv}/\tilde{R}^2}, \quad \rho(\boldsymbol{x}_\perp, t) = \frac{\tilde{\rho}(\tilde{\boldsymbol{x}}_\perp, \tilde{t})}{\tilde{\rho}_a}, \tag{2.2}$$

with $\boldsymbol{x}_\perp = (x, y)$ the horizontal coordinates, $p(\boldsymbol{x}_\perp, t)$ the fluid pressure relative to the ambient pressure, and $\rho(\boldsymbol{x}_\perp, t)$ the fluid density.

We consider small aspect ratios, $\varepsilon_{\rm bv} \ll 1$, for which the viscous flow in the thin layer separating the sheet and the wall dominates the system dynamics. Two other dimensionless numbers describe the flow. Inertial effects are characterised by the film Reynolds number $\mathrm{Re}_{\rm bv} = \tilde{\rho}\tilde{\omega}\tilde{H}_{\rm bv}^2/\tilde{\mu}$ that compares the inertial pressure $\tilde{\rho}\tilde{R}^2\tilde{\omega}^2$, with $\tilde{\omega}\tilde{R}$ the scale for the horizontal velocity, to the viscous stress $\tilde{F}_{\rm bv}/\tilde{R}^2$. The Reynolds number can also be written as $\mathrm{Re}_{\rm bv} = (\tilde{H}_{\rm bv}/\tilde{\delta})^2$, with $\tilde{\delta} = (\tilde{\mu}/\tilde{\rho}\tilde{\omega})^{1/2}$ the viscous penetration length, the lengthscale for diffusion of vorticity. It may also be

interpreted as a Womersley number, and we refer to appendix A.1 for a detailed discussion of the scaling of inertial effects. We only emphasise here that $\mathrm{Re}_{\mathrm{bv}}$ is constructed based on the vertical length and velocity scales, $\tilde{H}_{\mathrm{bv}}$ and $\tilde{\omega}\tilde{H}_{\mathrm{bv}}$, as appropriate in the lubrication limit $\varepsilon_{\mathrm{bv}} \ll 1$ (Batchelor 1967). Compressible effects are characterised by the Squeeze number $\mathrm{Sq}_{\mathrm{bv}} = \tilde{F}_{\mathrm{bv}}/\tilde{p}_a\tilde{R}^2$ that compares the viscous stress to the ambient pressure $\tilde{p}_a$ (Taylor & Saffman 1957). With (2.1), the inertial and compressible effects in the fluid are quantified, respectively, by

$$\mathrm{Re}_{\mathrm{bv}} = \frac{\tilde{\rho}_a\tilde{\omega}^2\tilde{R}^4}{\left(\tilde{\mu}\tilde{\omega}\tilde{B}^2\right)^{1/3}}, \qquad \mathrm{Sq}_{\mathrm{bv}} = \frac{\left(\tilde{\mu}\tilde{\omega}\tilde{B}^2\right)^{1/3}}{\tilde{p}_a\tilde{R}^2}. \tag{2.3}$$

2.2. *Inertial lubrication*

Let us find a depth-integrated description of the flow in the thin gap between the sheet and the wall ($\varepsilon_{\mathrm{bv}} \ll 1$) which includes the first-order effects of inertia at $\mathcal{O}(\mathrm{Re}_{\mathrm{bv}})$ and compressibility at $\mathcal{O}(\mathrm{Sq}_{\mathrm{bv}})$. Mass conservation yields

$$\frac{\partial(\rho h)}{\partial t} + \boldsymbol{\nabla}_\perp \cdot (\rho \boldsymbol{q}) = 0, \tag{2.4a}$$

$$\rho = 1 + \mathrm{Sq}_{\mathrm{bv}} p, \tag{2.4b}$$

with $\boldsymbol{q} = \int_0^h \boldsymbol{v}_\perp \mathrm{d}z = \tilde{\boldsymbol{q}}/\tilde{\omega}\tilde{L}$ the horizontal volumetric fluid flux, $\boldsymbol{v}_\perp$ the horizontal fluid velocity profile, and $\boldsymbol{\nabla}_\perp = (\partial/\partial x, \partial/\partial y)$ the horizontal gradient operator. Equation (2.4*b*) is the dimensionless ideal gas law assuming isothermal conditions, $\tilde{\rho}/\tilde{\rho}_a = 1 + \tilde{p}/\tilde{p}_a$, an assumption we discuss later in §5. The volumetric flux $\boldsymbol{q}$ appearing in (2.4) is found from the Navier-Stokes equations. Rojas *et al.* (2010) describe a procedure to consider the first-order inertial corrections to lubrication theory for free surface flows with $\varepsilon_{\mathrm{bv}} \ll 1$, $\mathrm{Re}_{\mathrm{bv}} \ll 1$. We adapt their derivation to a fluid layer bounded by two solid walls (appendix A), which yields the depth-integrated horizontal momentum balance, to $\mathcal{O}(\varepsilon_{\mathrm{bv}}^2, \mathrm{Re}_{\mathrm{bv}}, \varepsilon_{\mathrm{bv}}^2\mathrm{Re}_{\mathrm{bv}}, \mathrm{Re}_{\mathrm{bv}}\mathrm{Sq}_{\mathrm{bv}}, \mathrm{Sq}_{\mathrm{bv}})$:

$$12\boldsymbol{q} + h^3\boldsymbol{\nabla}_\perp p + \mathrm{Re}_{\mathrm{bv}} h^3 \left[\frac{6}{5}\frac{\partial}{\partial t}\left(\frac{\boldsymbol{q}}{h}\right) + \frac{54}{35}\frac{\boldsymbol{q}}{h}\cdot\boldsymbol{\nabla}_\perp\left(\frac{\boldsymbol{q}}{h}\right) - \frac{6}{35}\frac{\boldsymbol{q}}{h^2}\frac{\partial h}{\partial t}\right] = 0. \tag{2.5}$$

The first two terms in (2.5) encompass the Reynolds equation from inertialess lubrication theory, valid for vanishing Reynolds number (Batchelor 1967). The term proportional to $\mathrm{Re}_{\mathrm{bv}}$ corresponds to the first-order correction due to both the unsteady and convective inertia of the fluid. It corrects the parabolic Poiseuille velocity profile of lubrication theory and predicts a sextic velocity profile, discussed in §4. Rojas *et al.* (2010) found good agreement between experiments and this extended lubrication theory for Reynolds numbers of order one. Previous theoretical works from Ishizawa (1966) and Jones & Wilson (1975), albeit limited to non-deformable boundaries, suggest that this first-order correction may even be valid as long as the Reynolds number is less than 100. Equation (2.5) recovers the inertial corrections derived in these studies and generalises them to an arbitrary height $h(\boldsymbol{x}_\perp, t)$, suggesting that (2.5) may be valid for finite, relatively large, values of $\mathrm{Re}_{\mathrm{bv}}$, say $\mathcal{O}(10)$.

2.3. *Elastic deformations*

To close the system formed by (2.4) and (2.5), the fluid pressure p must be linked to elastic stresses by considering a vertical momentum balance of the elastic sheet. We

adopt the Kirchhoff-Love model (Timoshenko & Woinowsky-Krieger 1959; Landau & Lifshitz 1986) to describe the deformation of the sheet. We therefore neglect any in-plane stretching, which is justified for a sheet undergoing cylindrical bending, i.e., deforming in a single direction and preserving a zero Gaussian curvature (in which case the model reduces to the Euler-Bernoulli beam) and for two-dimensional deformations whose amplitude remains small compared to the thickness of the sheet. We also neglect the tension induced by the shear stress from the flow (Poulain *et al.* 2025). The normal force per unit area from the aerodynamic interactions in the thin gap is $p + \mathcal{O}(\varepsilon_{\mathrm{bv}}^2)$, so that the force balance in the thin-film limit reads:

$$\begin{aligned} \mathcal{I}_{\mathrm{bv}} \frac{\partial^2 h}{\partial t^2} &= p + \boldsymbol{\nabla}_\perp \cdot (\boldsymbol{\nabla}_\perp \cdot \mathbf{M}) + f_a(\boldsymbol{x}_\perp, t) + \mathcal{G} + f_w(h), \\ \mathbf{M} &= -\left[(1-\nu)\,\boldsymbol{\kappa} + \nu\,\mathrm{tr}(\boldsymbol{\kappa})\mathbf{I}\right]. \end{aligned} \tag{2.6}$$

The dimensionless number $\mathcal{I}_{\mathrm{bv}} = \tilde{\rho}_s \tilde{e} \tilde{H}_{\mathrm{bv}} \tilde{\omega}^2 \tilde{R}^2 / \tilde{F}_{\mathrm{bv}}$ compares solid inertia to the elastohydrodynamic stress scale. The right-hand-side of (2.6) corresponds respectively to the stress from the fluid, the bending stress (with $\boldsymbol{\kappa}$ the Hessian of h—the curvatures of the sheet), the periodic active stress f_a, the sheet's areal weight with $\mathcal{G} = \tilde{\rho}_s \tilde{e} \tilde{R}^2 \tilde{g} / \tilde{F}_{\mathrm{bv}} > 0$, and a term preventing collision with the wall. We also note that in the case of a constant bending rigidity considered here, the bending stresses simplify to $\boldsymbol{\nabla}_\perp \cdot (\boldsymbol{\nabla}_\perp \cdot \mathbf{M}) = -\nabla_\perp^4 h$. We emphasise that the sheet is assumed to have a uniform weight: $\mathcal{G}$ is constant. This differs from the experiments of Colasante (2016) and Weston-Dawkes *et al.* (2021), where it is heavier at its centre and may be submitted to an additional pulling force. We have made this choice to isolate the role of elastohydrodynamics without introducing additional complications. Nonetheless, this model is versatile, and non-uniform loading could be studied by prescribing a spatially-varying mass distribution $\mathcal{G}(\boldsymbol{x}_\perp)$, leading also to a spatially-varying inertia $\mathcal{I}_{\mathrm{bv}}(\boldsymbol{x}_\perp)$, and/or by adding a localised force to (2.6) .

The active forcing behind f_a is harmonic in time and is distributed at the centre of the sheet with a dimensionless radius $\ell = \tilde{l}/\tilde{R}$ (figure 1). Letting $\mathbb{H}$ the Heaviside function and $\alpha = \tilde{F}_a / \tilde{F}_{\mathrm{bv}}$ the dimensionless strength of the forcing, we have

$$f_a(\boldsymbol{x}_\perp, t) = \alpha \cos(t) \frac{1 - \mathbb{H}(|\boldsymbol{x}_\perp| - \ell)}{\ell}. \tag{2.7}$$

With (2.1), the dimensionless numbers in (2.6) read

$$\mathcal{I}_{\mathrm{bv}} = \frac{\tilde{\rho}_s \tilde{e} \tilde{\omega}^2 \tilde{R}^4}{\tilde{B}}, \quad \mathcal{G} = \frac{\tilde{F}_g}{\tilde{F}_{\mathrm{bv}}} = \frac{\tilde{\rho}_s \tilde{e} \tilde{g} \tilde{R}^2}{\left(\tilde{\mu} \tilde{\omega} \tilde{B}^2\right)^{1/3}}, \quad \alpha = \frac{\tilde{F}_a}{\tilde{F}_{\mathrm{bv}}} = \frac{\tilde{F}_a}{\left(\tilde{\mu} \tilde{\omega} \tilde{B}^2\right)^{1/3}}. \tag{2.8}$$

Finally, as discussed later in §3.2, we observe that when the forcing and weight both exceed a critical value, the edges of the sheet may contact the wall. To handle this numerically, we introduce a local repulsive force $f_w(h) = (A/h)^n$, $n > 1$, modeling an elastic collision with a contact that effectively occurs at the dimensionless height $A \ll 1$. Indeed, f_w is conservative, since it derives from the potential $A^n h^{1-n}/(n-1)$, and is only significant for $h \lesssim A$. The introduction of a short-ranged repulsion is similar to the penalty method commonly employed in contact mechanics (Wriggers 2006) and in fluid-structure interaction problems (e.g. Glowinski *et al.* 2001).

2.4. *Timescales*

To discuss the different physical effects that contribute to the lubrication dynamics, it will prove useful to define characteristic timescales associated with each mechanism. From the viscous lubrication equation (2.4) and (2.5) with $\mathrm{Re}_{\mathrm{bv}} = \mathrm{Sq}_{\mathrm{bv}} = 0$, $12\tilde{\mu}\partial\tilde{h}/\partial\tilde{t} = \tilde{\boldsymbol{\nabla}}_\perp \cdot (\tilde{h}^3\tilde{\boldsymbol{\nabla}}_\perp\tilde{p})$, a timescale $\tilde{T} = \tilde{\mu}\tilde{R}^2/(\tilde{H}^2\tilde{P})$ can be defined with $\tilde{H}$ a height and $\tilde{P}$ the characteristic pressure associated with the mechanism of interest. Considering each effect separately, this defines the following timescales:

$$\text{gravitational}: \quad \tilde{T}_g(\tilde{h}) = \frac{\tilde{\mu}\tilde{R}^2}{\tilde{\rho}_s\tilde{g}\tilde{e}\tilde{h}^2}, \tag{2.9a}$$

active: $\tilde{T}_a(\tilde{h}) = \tilde{\mu}\tilde{R}^4/(\tilde{F}_a\tilde{h}^2)$, elastohydrodynamic: $\tilde{T}_{\mathrm{bv}}(\tilde{h}) = \tilde{\mu}\tilde{R}^6/(\tilde{B}\tilde{h}^3)$, compressible: $\tilde{T}_c(\tilde{h}) = \tilde{\mu}\tilde{R}^2/\tilde{p}_a\tilde{h}^2$, and inertial: $\tilde{T}_i(\tilde{h}) = \tilde{\rho}_a\tilde{h}^2/\tilde{\mu}$. The latter is characteristic of momentum diffusion and is not defined by the same lubrication scaling. While gravity always acts, the effects of elasticity, compressibility, and inertia are only relevant when the sheet is forced into motion by the active force. In these cases, we expect the time-averaged and long-term dynamic of the sheet to only depend on even powers of the active force $\tilde{F}_a$, since a change of sign of the force magnitude $\tilde{F}_a$ is equivalent to a phase shift. We therefore define visco-active timescales as the square of the active forcing timescale $\tilde{T}_a$ divided by the response timescale of the mechanism of interest:

$$\text{elastohydrodynamic: } \tilde{T}_{\mathrm{a,bv}}(\tilde{h}) = \frac{\tilde{T}_a^2(\tilde{h})}{\tilde{T}_{\mathrm{bv}}(\tilde{h})} = \frac{\tilde{\mu}\tilde{R}^2\tilde{B}}{\tilde{F}_a^2\tilde{h}},$$

$$\text{inertial: } \tilde{T}_{\mathrm{a,i}}(\tilde{h}) = \frac{\tilde{T}_a^2(\tilde{h})}{\tilde{T}_i(\tilde{h})} = \frac{\tilde{\mu}^3\tilde{R}^8}{\tilde{F}_a^2\tilde{\rho}_a\tilde{h}^6}, \quad \text{compressible: } \tilde{T}_{\mathrm{a,c}}(\tilde{h}) = \frac{\tilde{T}_a^2(\tilde{h})}{\tilde{T}_c(\tilde{h})} = \frac{\tilde{\mu}\tilde{R}^6\tilde{p}_a}{\tilde{F}_a^2\tilde{h}^2}. \tag{2.9b}$$

2.5. *Boundary conditions*

The edges of the elastic sheet are free of bending moment, twisting moment, and shear force. The appropriate boundary conditions are (Naghdi 1973, p. 586):

$$\mathbf{M}\boldsymbol{e_r} \cdot \boldsymbol{e_r} = 0, \quad (\boldsymbol{\nabla}_\perp \cdot \mathbf{M}) \cdot \boldsymbol{e_r} + \boldsymbol{\nabla}_\perp (\mathbf{M}\boldsymbol{e_r} \cdot \boldsymbol{e_\theta}) \cdot \boldsymbol{e_\theta} = 0, \tag{2.10}$$

where $\boldsymbol{e_r}$ is the outward unit normal at the edge of the sheet and $\boldsymbol{e_\theta}$ is the tangent. As the third and final boundary condition, we set the pressure at the edges of the sheet as

$$p = \begin{cases} 0 & \text{if } \boldsymbol{q}\cdot\boldsymbol{e}_r > 0 \quad \text{(outflow)} \\ -\dfrac{k}{2}\mathrm{Re}_{\mathrm{bv}}\left(\dfrac{\boldsymbol{q}\cdot\boldsymbol{e}_r}{h}\right)^2 & \text{if } \boldsymbol{q}\cdot\boldsymbol{e}_r < 0 \quad \text{(inflow)} \end{cases}, \tag{2.11}$$

with $k = 1/2$, a loss coefficient. This boundary condition models the pressure loss when fluid enters the thin gap; it is justified and discussed in more detail in Appendix B. In the inertialess case $\mathrm{Re}_{\mathrm{bv}} = 0$, (2.11) simplifies to the classical condition $p = 0$ which imposes the ambient pressure at the edges.

2.6. *Numerical model*

We have formulated the governing equations (2.4*a*), (2.5), (2.6) and boundary conditions (2.10) and (2.11) for a 2-dimensional (2D) sheet for completeness. For purely

viscous flows, we have shown (Poulain *et al.* 2025) that there are no qualitative differences between the 1D and 2D axisymmetric situations. Accordingly, we restrict the present study to 1D for simplicity. Hence, we consider $\boldsymbol{x}_\perp \to x$ and $\partial/\partial y = 0$. We solve the governing equations in conservative form

$$\frac{\partial \boldsymbol{S}}{\partial t} + \frac{\partial \boldsymbol{F}}{\partial x} = \boldsymbol{Q}, \tag{2.12a}$$

with

$$\begin{aligned}
\boldsymbol{S}(\boldsymbol{U}) &= [\,\rho h, && \mathcal{I}_{\mathrm{bv}} v, && 0, && \frac{6\mathrm{Re}_{\mathrm{bv}}}{5} u, && h\,],\\
\boldsymbol{F}(\boldsymbol{U}) &= [\,0, && -\frac{\partial m}{\partial x}, && -\frac{\partial h}{\partial x}, && \frac{27}{35}\mathrm{Re}_{\mathrm{bv}} u^2 + p, && hu\,],\\
\boldsymbol{Q}(\boldsymbol{U}) &= [\,\rho v, && p + f_a(x,t) + \mathcal{G} + f_w(h), && m, && -\frac{12u}{h^2} + \frac{6}{35}\mathrm{Re}_{\mathrm{bv}}\frac{uv}{h}, && 0\,],
\end{aligned}$$

and the five primary unknowns $\boldsymbol{U} = [v, m, h, u, p]$, representing the vertical sheet velocity $v = \partial h/\partial t$, bending moment $m = -\partial^2 h/\partial x^2$, height h, average horizontal fluid velocity $u = q/h$, and fluid pressure p, respectively. We note that $\rho = 1 + \mathrm{Sq}_{\mathrm{bv}} p$.

We consider a domain $x \in [0, 1]$ with symmetric boundary conditions at $x = 0$ and the appropriate boundary conditions at $x = 1$:

$$m = 0, \quad \frac{\partial m}{\partial x} = 0, \quad p = \begin{cases} 0 & \text{if } u \geqslant 0, \\ -k\mathrm{Re}_{\mathrm{bv}} u^2/2 & \text{if } u < 0. \end{cases} \tag{2.12b}$$

We solve (2.12) using the DuMu^x library (Koch *et al.* 2021). We discretise space using a staggered finite volume scheme, where pressure unknowns are located at cell centres and other unknowns are located at vertices. This setup avoids checkerboard oscillations in the fluid pressure. The flux term in u^2 is treated with a first-order upwind scheme. The equations are advanced in time using a diagonally-implicit $3rd$-order Runge-Kutta scheme (Alexander 1977, Thm. 5), and the nonlinear system at each Runge-Kutta stage is solved with Newton's method. Lower-order methods either yielded unsatisfactory accuracy or required excessively small time step sizes. We used time step sizes $10^{-4} \leqslant \Delta t \leqslant 0.2$ and spatial step sizes $0.002 \leqslant \Delta x \leqslant 0.02$. The numerical simulations have been run to a time-averaged steady state–which could take from $t = \mathcal{O}(10)$ up to $t = \mathcal{O}(10^6)$ depending on the parameters– or until the height diverged. We systematically ensured that any divergence of the numerical solution was independent of the numerical parameters and therefore corresponded to adhesion failure. For initial conditions, we considered a flat sheet, $\boldsymbol{U}(x, t = 0) = [0, 0, h(x, t = 0), 0, 0]$, with $h(x, t = 0)$ a constant. For large values of α and $\mathcal{G}$, this initialisation sometimes leads to divergence, even though a time-averaged steady state exists. In these cases, we initialised the simulation using the steady-state solution from a run with the same α but smaller $\mathcal{G}$ (numerical continuation). The repulsion force was either turned off ($A = 0$) or, when needed, chosen as $f_w(h) = (A/h)^n$ with $A = 10^{-5}$ and $n = 5$. We have verified that this choice does not significantly affect the results as long as A is small and n is large.

2.7. *Choice of dimensionless parameters*

Equations (2.4) to (2.6) depend on five dimensionless numbers defined in (2.1) and (2.8), with $\varepsilon_{\mathrm{bv}}$ not appearing in the governing equations and ℓ defined in (2.7).

They are summarised in table 1. Since dimensional quantities such as the sheet's bending rigidity $\tilde{B}$ or the excitation frequency $\tilde{\omega}$ enter multiple dimensionless groups, independently varying them in experiments is not feasible. Nevertheless, numerical simulations enable us to disentangle the respective roles of the dimensionless numbers in the dynamics and to clarify the underlying physical mechanisms they influence. We consider a uniform sheet with a uniformly distributed weight: $\mathcal{I}_{\rm bv}$ and $\mathcal{G}$ are constants. We also consider the limit where the forcing is localised at a single point, $\ell \to 0$; in practice, we set $\ell = 0.05$ in our numerical simulations. The effect of a finite ℓ and a sheet locally rigid at its centre has already been discussed in prior work (Poulain *et al.* 2025).

To guide our study, we consider the experiments of Weston-Dawkes *et al.* (2021), who report a time-averaged equilibrium height (figure 1*b*) $\tilde{h}_{\rm eq} \approx 600\mu$m for a sheet of thickness $\tilde{e} \approx 300\mu$m, Young's modulus $\tilde{E} \approx 3$GPa, radius $\tilde{R} \simeq 10$cm, vibrating at frequency $\tilde{\omega} = 2\pi \times 200$Hz and supporting a weight $\tilde{W} \approx 5$N. The density ratio between the sheet and air is $\tilde{\rho}_s/\tilde{\rho}_a \approx 10^3$. The vibrations are generated by an eccentric rotating mass motor, with an estimated mass $\tilde{m} \approx 0.6$g and gyration radius $\tilde{r} \approx 1$mm, yielding a driving force $\tilde{F}_a = \tilde{m}\tilde{r}\tilde{\omega}^2$. This gives a dimensionless forcing strength $\alpha = \tilde{F}_a/\tilde{F}_{\rm bv} \approx 90$. While this is overestimated due to the rigid central support (Poulain *et al.* 2025), it nevertheless suggests that the regime $\alpha = \mathcal{O}(10)$ is relevant experimentally.

Although we consider a dynamics dominated by viscous forces, we are interested in corrections due to additional physical effects. From the above parameters, the heightscale is $\tilde{H}_{\rm bv} \approx 14$mm, while the dimensionless equilibrium height is only a small fraction of this value: $h_{\rm eq} = \tilde{h}_{\rm eq}/\tilde{H}_{\rm bv} \approx 0.04$. Our theoretical and numerical analysis will recover this observation. However, this shows that the dimensionless numbers based on $\tilde{H}_{\rm bv}$, such as $\mathrm{Re}_{\rm bv}$, $\mathrm{Sq}_{\rm bv}$, and $\mathcal{I}_{\rm bv}$, which allow for a compact theoretical description of the system dynamics, are not accurate indicators of the relative effect of fluid inertia, fluid compressibility, or solid inertia when the system is at equilibrium height. Hence, we additionally define dimensionless numbers using $\tilde{h}_{\rm eq}$ as the vertical scale:

$$\mathrm{Re}_{\rm eq} = \frac{\tilde{\rho}_a\tilde{\omega}\tilde{h}_{\rm eq}^2}{\tilde{\mu}} = h_{\rm eq}^2\mathrm{Re}_{\rm bv}, \quad \mathrm{Sq}_{\rm eq} = \frac{\tilde{\mu}\tilde{\omega}\tilde{R}^2}{\tilde{h}_{\rm eq}^2\tilde{p}_a} = h_{\rm eq}^{-2}\mathrm{Sq}_{\rm bv}, \quad \mathcal{I}_{\rm eq} = \frac{\tilde{\rho}_s\tilde{e}\tilde{h}_{\rm eq}^3\tilde{\omega}}{\tilde{\mu}\tilde{R}^2} = h_{\rm eq}^3\mathcal{I}_{\rm bv}. \tag{2.13}$$

Unlike the original dimensionless groups, these quantities cannot be computed a priori since $\tilde{h}_{\rm eq}$ is selected by the system and is initially unknown. The experimental values yield $\alpha = \mathcal{O}(10)$, and we systematically vary α in §3. The Reynolds number is $\mathrm{Re}_{\rm eq} \approx 30$, indicating that fluid inertia may play a significant role, studied in §4. We also note that in some of the experiments of Weston-Dawkes *et al.* (2021), when the sheet is steadily pulled instead of equilibrating under a constant load, the central height can reach up to 3 mm, corresponding to Reynolds numbers of several hundred. This further highlights the importance of understanding fluid inertial effects. The parameter controlling solid inertia, however, is smaller, $\mathcal{I}_{\rm eq} \approx 0.6$, suggesting a weaker yet potentially non-negligible effect of solid inertia. In this study, we focus on the influence of fluid effects and leave a systematic investigation of solid inertia for future work. A related investigation into the coupling between solid inertia within elastohydrodynamic systems can be found in Ramanarayanan & Sánchez (2024). Finally, although $\mathrm{Sq}_{\rm eq} \approx 0.006$, we show in §5 that compressibility can still noticeably affect the dynamics even for small Squeeze numbers.

Table 1: Characteristic scales and dimensionless parameters.

Symbol	Definition	Physical meaning	Unit
$\tilde{H}_{\mathrm{bv}}$	$\tilde{R}^2\left(\frac{\tilde{\mu}\tilde{\omega}}{\tilde{B}}\right)^{1/3}$	height balancing viscous and bending effects	m
$\tilde{F}_{\mathrm{bv}}$	$\left(\tilde{\mu}\tilde{\omega}\tilde{B}^2\right)^{1/3}$	force balancing viscous and bending effects	N
$\varepsilon_{\mathrm{bv}}$	$\tilde{H}_{\mathrm{bv}}/\tilde{R}$	aspect ratio	-
α	$\tilde{F}_a/\tilde{F}_{\mathrm{bv}}$	forcing amplitude/elastohydrodynamic	-
$\mathcal{G}$	$\frac{\tilde{\rho}_s\tilde{e}\tilde{g}\tilde{R}^2}{\tilde{F}_{\mathrm{bv}}}$	weight/elastohydrodynamic	-
$\mathcal{I}_{\mathrm{bv}}$	$\frac{\tilde{\rho}_s\tilde{e}\tilde{\omega}^2\tilde{R}^4}{\tilde{B}}$	solid inertia/elastohydrodynamic	-
$\mathrm{Re}_{\mathrm{bv}}$	$\frac{\tilde{\rho}_a\tilde{\omega}^2\tilde{R}^4}{\tilde{F}_{\mathrm{bv}}}$	fluid inertia/elastohydrodynamic	-
$\mathrm{Sq}_{\mathrm{bv}}$	$\frac{\tilde{F}_{\mathrm{bv}}}{\tilde{p}_a\tilde{R}^2}$	compressibility (elastohydrodynamic/atmospheric pressure)	-
ℓ	$\tilde{\ell}/\tilde{R}$	forcing size	-

3. Incompressible and inertialess analysis

3.1. *Weak active forcing ($\alpha \lesssim 1$)*

We first consider the regime for which inertia and compressibility are negligible, $\mathcal{I}_{\mathrm{bv}} = \mathrm{Re}_{\mathrm{bv}} = \mathrm{Sq}_{\mathrm{bv}} = 0$, so that the dynamics is solely governed by viscous elastohydrodynamic interactions. Then, the governing equations (2.4) and (2.5) simplify to the Reynolds equation describing inertialess incompressible lubrication flows:

$$12\frac{\partial h}{\partial t} - \boldsymbol{\nabla}_\perp \cdot \left(h^3 \boldsymbol{\nabla}_\perp p\right) = 0. \tag{3.1}$$

We studied this regime in (Poulain *et al.* 2025) in the limit $\alpha \lesssim 1$. More precisely, we used an asymptotic expansion to $\mathcal{O}(\alpha^2)$ and found the results valid up to $\alpha \simeq 1$. In short, when periodic vibrations drive an elastic sheet at its centre, it tends to adhere to a nearby surface due to the coupling between its elastic deformation and the lubrication flow in the intervening gap. As the sheet is pushed towards the surface, it adopts a convex shape that favours fluid outflow; while when it is pulled away from the surface, it adopts a concave shape that resists inflow (figure 2*a*). This asymmetry in the flow response over a period of oscillation results in a net inflow, leading to a time-averaged attraction toward the surface. More rigorously, this symmetry breaking can be traced back to the non-time-reversible pressure distribution in a rigid squeeze film (as shown later in figure 7*b*). When the soft sheet deforms under this pressure, its kinematics inherit the non-reversibility, so that the dynamics is no longer constrained by the scallop theorem (Purcell 1977; Lauga 2011). The resulting

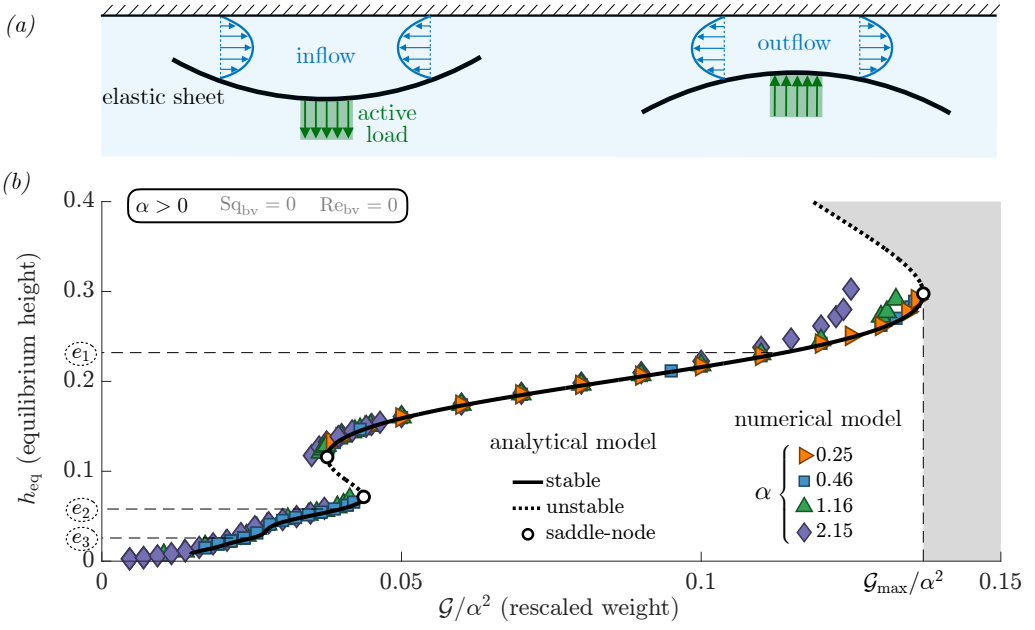

Figure 2: Asymptotic results for $\alpha \lesssim 1$, $\mathcal{I}_{\mathrm{bv}} = \mathrm{Re_{bv}} = \mathrm{Sq_{bv}} = 0$, adapted from Poulain *et al.* (2025). (*a*) Schematic illustration of the link between the active force direction and the sheet's convexity. (*b*) Equilibrium height h_{eq} as a function of the the rescaled dimensionless weight $\mathcal{G}/\alpha^2$. Symbols are results from numerical simulations, the lines are the prediction of (3.2) obtained by numerical continuation (with a cutoff $N = 5$). For $\mathcal{G}/\alpha^2 > \mathcal{G}_{\max}/\alpha^2 \simeq 0.137$, no equilibrium is possible and the sheet always detaches from the substrate (greyed area).

rectified flow can then counteract the sheet's weight and give rise to an equilibrium hovering height. We have used these insights to study the system analytically and present the conclusions of our analysis below. We refer the reader to appendix C for further details on the assumptions we have used, and to Poulain *et al.* (2025) for the complete derivation. In short, the height $h(x,t)$ is decomposed into spatial eigenmodes, and an asymptotic analysis allows to find an evolution equation for time-averaged height $\langle h_0\rangle(t) = \int_t^{t+2\pi} h(x=0,t')\,\mathrm{d}t'$ at $\mathcal{O}(\alpha^2)$:

$$\frac{1}{\alpha^2\langle h_0\rangle^2}\frac{\mathrm{d}\langle h_0\rangle}{\mathrm{d}t} = \frac{1}{4}\frac{\mathcal{G}}{\alpha^2}\langle h_0\rangle - d_0 + \sum_{i,j=1}^{\infty} d_{ij} g_{ij}\left(\langle h_0\rangle\right), \tag{3.2a}$$

$$g_{ij}(h) = \frac{1+\left(\dfrac{h}{\sqrt{e_i e_j}}\right)^6}{\left(1+\left(\dfrac{h}{e_i}\right)^6\right)\left(1+\left(\dfrac{h}{e_j}\right)^6\right)}.$$

In dimensional units, this can be expressed compactly using the gravitational timescale $\tilde{T}_g$ and the active elastohydrodynamic timescale $\tilde{T}_{\mathrm{a,bv}}$ introduced in (2.9):

$$\begin{aligned}\frac{\mathrm{d}\langle\tilde{h}_0\rangle}{\mathrm{d}\tilde{t}} &= \frac{1}{4}\frac{\tilde{\rho}_s\tilde{g}\tilde{e}\langle\tilde{h}_0\rangle^3}{\tilde{\mu}\tilde{R}^2} + \frac{\tilde{F}_a^2\langle\tilde{h}_0\rangle^2}{\tilde{\mu}\tilde{R}^2\tilde{B}}\left[-d_0 + \sum_{i,j=1}^{\infty} d_{ij}g_{ij}\left(\frac{\langle\tilde{h}_0\rangle}{\tilde{H}_{\mathrm{bv}}}\right)\right] \\ &= \frac{1}{4}\frac{\langle\tilde{h}_0\rangle}{\tilde{T}_g\left(\langle\tilde{h}_0\rangle\right)} + \frac{\langle\tilde{h}_0\rangle}{\tilde{T}_{\mathrm{a,bv}}\left(\langle\tilde{h}_0\rangle\right)}\left[-d_0 + \sum_{i,j=1}^{\infty} d_{ij}g_{ij}\left(\frac{\langle\tilde{h}_0\rangle}{\tilde{H}_{\mathrm{bv}}}\right)\right].\end{aligned} \tag{3.2b}$$

The first two terms on the right-hand side of (3.2) correspond respectively to the effect of gravity, where we assumed $\mathcal{G}/\alpha^2 = \mathcal{O}(1)$, and to the first-order effect of elastohydrodynamics, with $d_0 = 0.0122$. The third term corresponds to the effects of the eigenmodes ζ_i (shown in figure 11) on the dynamics, with the $e_i = 0.242/i^2$, characteristic dimensionless heights corresponding to the height scale below which the i-th mode ζ_i is excited. This means that we predict higher-order excitation modes as the sheet approaches the wall. The d_{ij} are numerical coefficients of the symmetric matrix d_{ij} characterising the strength of the effect of mode i ($i = j$) or of the coupling between modes i and j on the dynamics; their values are given in appendix C.

The bifurcation diagram of (3.2) is shown in figure 2(b). If the rescaled weight is too large, $\mathcal{G} > \mathcal{G}_{\max} = 0.137\alpha^2$, there is no equilibrium and the sheet fails to adhere: gravity overcomes the adhesive elastohydrodynamic effect and $\langle h_0\rangle \to \infty$. For $0 < \mathcal{G} < \mathcal{G}_{\max}$, the sheet finds an equilibrium near the wall, $\langle h_0\rangle \to h_{\mathrm{eq}}$. We show in figure 2($b$) that numerical simulations of the governing equations (2.6) and (3.1) agree remarkably well with the bifurcation diagram of the reduced model (3.2) for $\alpha \lesssim 1$.

To study the sheet's deformations numerically, we consider the time-averaged equilibrium and let

$$h(x,t) = h_d(x,t) + \langle h\rangle(x,t) + \bar{h}(t) - h_{\mathrm{eq}}, \tag{3.3}$$

where $\langle h\rangle(x,t) = (1/2\pi)\int_t^{t+2\pi} h(x,t')\,\mathrm{d}t'$ is the time average (independent of time once a time-averaged steady state is reached), $\bar{h}(t) = (1/2)\int_{-1}^{1} h(x',t)\,\mathrm{d}x'$ is the spatial average, and $h_{\mathrm{eq}} = \langle\bar{h}\rangle$ the time- and space-averaged height. The function $h_d(x,t)$ then represent the periodic deformations to the static shape $\langle h\rangle(x)$, with $\langle h_d\rangle = \bar{h}_d = 0$. The decomposition (3.3) is illustrated in figure 3(a), where we also show examples of deformations from numerical simulations in panels ($b-d$). This illustrates that higher-order modes of deformation are indeed excited as $\mathcal{G}/\alpha^2$ and h_{eq} decrease.

Finally, our analysis shows that for $\alpha \lesssim 1$ the maximum supported weight $\mathcal{G}_{\max}$ scales as α^2. Coming back to dimensional quantities gives $\tilde{W}_{\max} \sim \tilde{F}_a^2/\tilde{F}_{\mathrm{bv}}$, with $\tilde{F}_{\mathrm{bv}}$ the elastohydrodynamic force scale and $\tilde{F}_a$ the active force. This predicts that for a given forcing amplitude $\tilde{F}_a$, an increasingly soft sheet would sustain arbitrarily large weights $\tilde{W}_{\max}$. However, as the sheet becomes softer ($\tilde{F}_{\mathrm{bv}}$ decreases), $\alpha = \tilde{F}_a/\tilde{F}_{\mathrm{bv}}$ increases and cannot be considered small anymore. We study this second regime next.

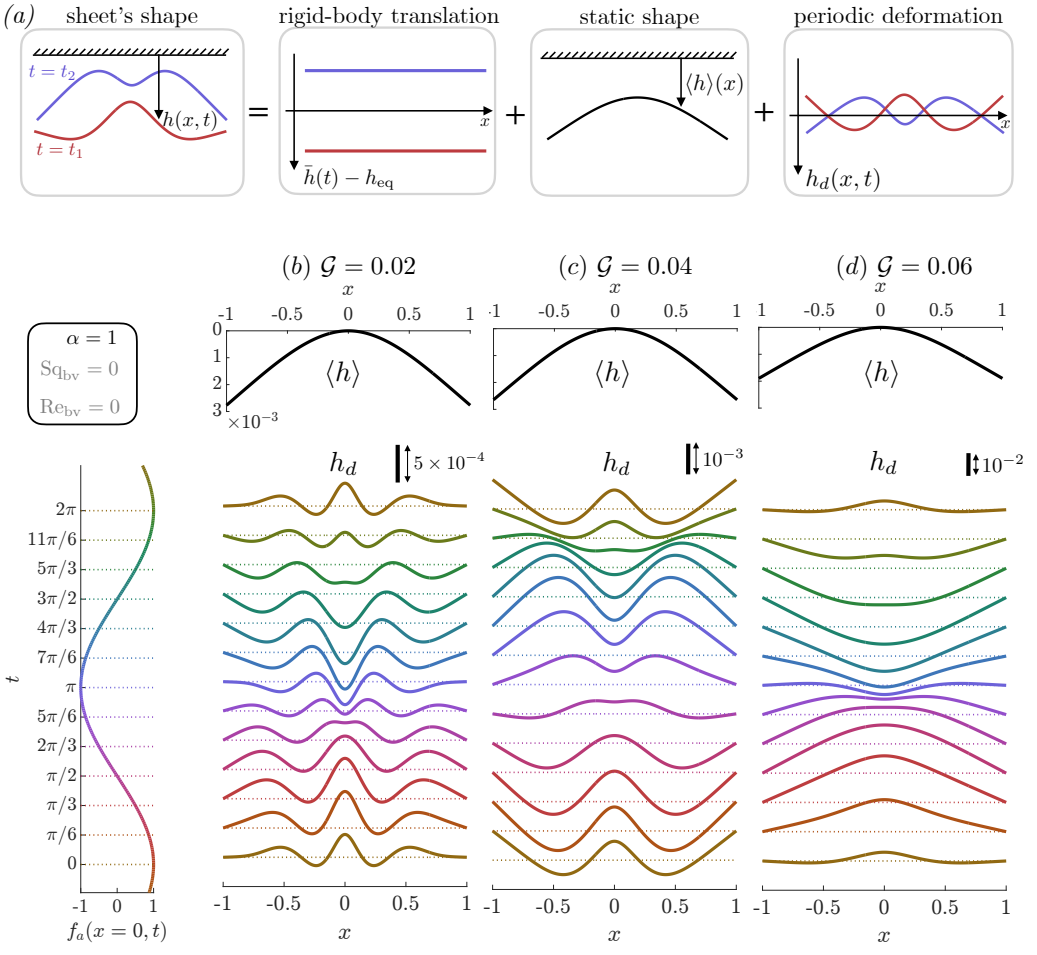

Figure 3: (*a*) Illustration of the decomposition (3.3) of the sheet's shape into a rigid-body translation $\bar{h}(t) - h_{\rm eq}$, a static shape $\langle h \rangle(x)$ (independent of time at the time-averaged steady state), and a time-periodic deformation $h_d(x,t)$. (*b, c, d*) Time-averaged shape $\langle h \rangle$ and the periodic deformation h_d for $G = 0.02,\ 0.04,\ 0.06$, respectively, and $\alpha = 1$, $\mathcal{I}_{\rm bv} = \mathrm{Re_{bv}} = \mathrm{Sq_{bv}} = 0$. These are obtained from numerical simulations at the time-averaged steady state. h_d is shown at various times of one vibration cycle, with scale bars showing the amplitude of the deformations. As G and correspondingly $h_{\rm eq}$ decrease, higher-order vibration modes are excited.

3.2. *Strong active forcing ($\alpha \gg 1$)*

3.2.1. *Contactless adhesion – Maximum supported weight*

We show in figure 4(*a, b*) bifurcation diagrams obtained by numerically solving the governing equations (2.6) and (3.1) for $0 < \alpha \leqslant 100$, $\mathcal{I}_{\rm bv} = \mathrm{Re_{bv}} = \mathrm{Sq_{bv}} = 0$. The corresponding regime map of accessible dimensionless weight is shown in figure 4(*c*) and reveals three distinct regions: (i) a regime where adhesion is not possible and the system fails, (ii) a regime of contactless adhesion, and (iii) a regime where we predict adhesion but with the sheet's edges periodically touching the substrate. The latter effect is discussed in §3.2.4; we first focus on contactless adhesion. For a given

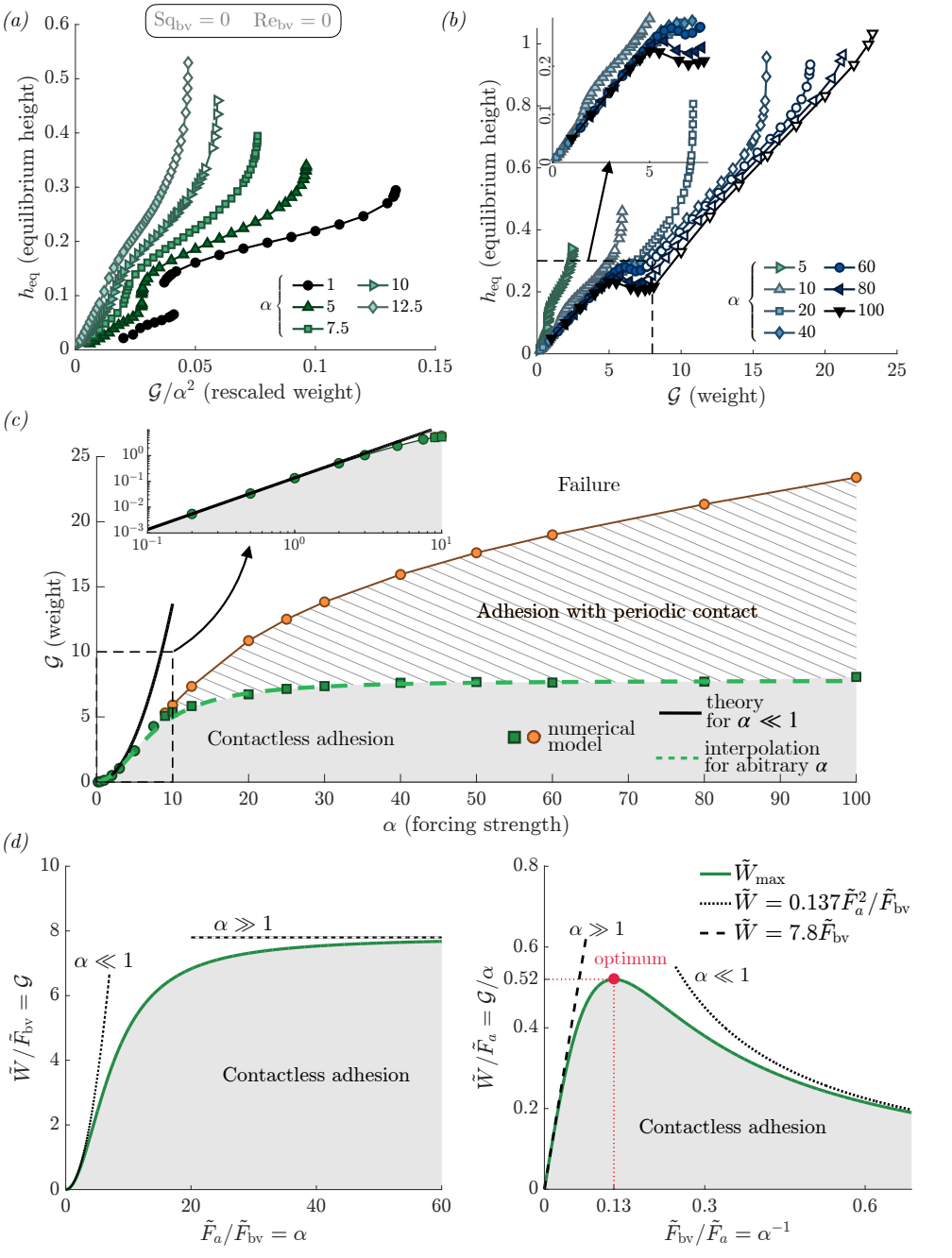

Figure 4: Varying active forcing α for an inertialess and incompressible system, $\mathcal{I}_{\mathrm{bv}} = \mathrm{Re_{bv}} = \mathrm{Sq_{bv}} = 0$. (a, b) Equilibrium height as a function of the dimensionless weight. As α increases, the scaling $\mathcal{G}_{\max} \sim \alpha^2$ does not collapse the data anymore. Open symbols represent cases where contact occurs at the edges of the sheet. (c) Regime map showing the three different possibilities (adhesion with or without edge contact, and adhesion failure) as a function of the dimensionless weight and forcing. The solid line represents the prediction $\mathcal{G}_{\max} = 0.137\alpha^2$ derived for $\alpha \ll 1$, and the dashed line is the interpolation (3.4). The inset is a zoom near the origin on a logarithmic scale. (d) Regime maps from (3.4) as $\tilde{F}_a$ varies for fixed $\tilde{F}_{\mathrm{bv}}$ (left), and $\tilde{F}_{\mathrm{bv}}$ varies for fixed $\tilde{F}_a$ (right).

α, we define $\mathcal{G}_{\max}$ as the threshold weight above which contactless adhesion cannot take place.

We see in figure 4(*c*) that the relation $\mathcal{G}_{\max} = 0.137\alpha^2$ is well verified for $\alpha \lesssim 1$, but that $\mathcal{G}_{\max}$ reaches an approximately constant value of 7.8 for $\alpha \gtrsim 20$. These two asymptotic behaviours are captured by the following interpolation, which also describes well the data over the whole range $0 < \alpha \leqslant 100$ (figure 4*c*):

$$\mathcal{G}_{\max} \simeq 0.137\frac{\alpha^2}{1+0.0176\alpha^2}, \quad \tilde{W}_{\max} \simeq 0.137\frac{\tilde{F}_a^2/\tilde{F}_{\mathrm{bv}}}{1+0.0176\tilde{F}_a^2/\tilde{F}_{\mathrm{bv}}^2}. \tag{3.4}$$

In dimensional quantities, we find $\tilde{W}_{\max} = 0.137\tilde{F}_a^2/\tilde{F}_{\mathrm{bv}}$ for $\tilde{F}_a \lesssim \tilde{F}_{\mathrm{bv}}$ (weak forcing), and $\tilde{W}_{\max} \simeq 7.8\tilde{F}_{\mathrm{bv}}$ for $\tilde{F}_a \gg \tilde{F}_{\mathrm{bv}}$ (strong forcing). In other words, if the forcing is strong enough, the maximum supported weight becomes independent of the forcing amplitude and scales as $\tilde{F}_{\mathrm{bv}}$. Equation (3.4) is consistent with the symmetry of the system: the long-term, time-averaged behaviour can only depend on even powers of α or $\tilde{F}_a$, as reversing the sign of the forcing is equivalent to a mere phase shift. It is also worth noting that the regimes of weak and strong forcing correspond to small and large deformations, respectively, of the sheet with respect to $\tilde{h}_{\mathrm{eq}}$. In other soft lubrication problems, these two limits also lead to different scalings (Essink *et al.* 2021).

Equation (3.4) provides valuable insights into the evolution of the maximum supported weight $\tilde{W}_{\max}$ with the forcing and material parameters, as shown in figure 4(*d*). At fixed $\tilde{F}_{\mathrm{bv}}$ (left panel), increasing the forcing strength initially enhance adhesion, but $\tilde{W}_{\max}$ saturates beyond $\tilde{F}_a/\tilde{F}_{\mathrm{bv}} \approx 10$. Conversely, at fixed $\tilde{F}_a$ (right panel), softening the sheet by decreasing $\tilde{F}_{\mathrm{bv}}$ first increases the maximum weight, before weakening adhesion. This shows an optimum at $\tilde{F}_{\mathrm{bv}}^\star = (\tilde{\mu}\tilde{\omega}\tilde{B}^2)^\star \approx 0.13\tilde{F}_a$, with an associated bending stiffness $\tilde{B}^\star \approx 0.05\tilde{F}_a^{3/2}\,(\tilde{\mu}\tilde{\omega})^{-1/2}$. This also corresponds to an optimal forcing frequency, although its expression depends on the actuator, whose properties set the relation between $\tilde{\omega}$ and $\tilde{F}_a$. If $\tilde{F}_{\mathrm{bv}}$ and $\tilde{F}_a$ can be tuned independently, the largest $\tilde{W}_{\max}$ is achieved by maximising $\tilde{F}_a$. In practice, this means using the most powerful available actuator and adjusting the sheet's bending rigidity accordingly. Practical design would also need to account for energy consumption and for the fact that powerful vibration motors are typically both heavy and bulky; their lateral extent also limits adhesion (Poulain *et al.* 2025). Nevertheless, our prediction resonates qualitatively with experimental observations: using relatively small motors, Weston-Dawkes *et al.* (2021) demonstrated $\tilde{W}_{\max} \approx 5$ N using thin and soft sheets, while experiments by Colasante (2016) (see also experiments from the same author reported by Ramanarayanan & Sánchez (2024)) show $\tilde{W}_{\max} = \mathcal{O}(100\mathrm{N})$ using stronger motors attached to stiffer sheets.

3.2.2. *Contactless adhesion – Equilibrium height*

We observe a remarkable linear relationship between h_{eq} and $\mathcal{G}$ for $\alpha \gg 1$ in the inset of figure 4(*b*), for $\mathcal{G} \lesssim \mathcal{G}_{\max}$. Combining this observation with the asymptotic results of the previous section, we find:

$$h_{\mathrm{eq}} \approx \begin{cases} f\left(\dfrac{\mathcal{G}}{\alpha^2}\right) & \text{if} \quad \alpha \lesssim 1, \\ 0.05\mathcal{G} & \text{if} \quad \alpha \gg 1, \end{cases} \qquad \text{for } \mathcal{G} \lesssim \mathcal{G}_{\max}. \tag{3.5a}$$

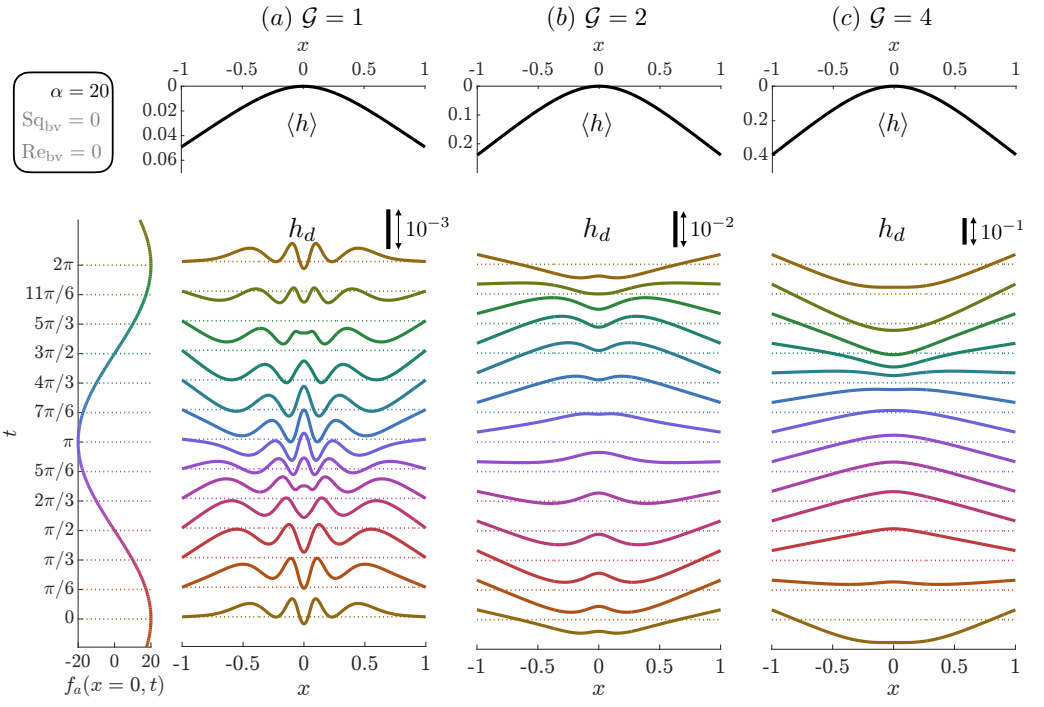

Figure 5: Time-averaged shape $\langle h \rangle$ and the periodic deformation h_d for $\alpha = 20$, $\mathcal{I}_{\mathrm{bv}} = \mathrm{Re_{bv}} = \mathrm{Sq_{bv}} = 0$, and $\mathcal{G} = 1,\ 2,\ 4$ in (a, b, c), respectively.

or, in dimensional units,

$$\tilde{h}_{\mathrm{eq}} \approx \begin{cases} \tilde{H}_{\mathrm{bv}} \times f\left(\dfrac{\tilde{W}\tilde{F}_{\mathrm{bv}}}{\tilde{F}_a^2}\right) & \text{if} \quad \tilde{F}_a \lesssim \tilde{F}_{\mathrm{bv}}, \\ 0.05\dfrac{\tilde{W}\tilde{R}^2}{\tilde{B}} & \text{if} \quad \tilde{F}_a \gg \tilde{F}_{\mathrm{bv}} \end{cases} \qquad \text{for } \tilde{W} \lesssim \tilde{W}_{\max}, \tag{3.5b}$$

with the maximum weight given by (3.4). The function f represents the stable fixed points of (3.2) and is shown in figure 2(*a*); its analytical approximations are discussed by Poulain *et al.* (2025). Equation (3.5*b*) shows that, for strong forcing $\alpha \gg 1$, the equilibrium height results from a balance between the bending force and gravity, with viscosity setting the maximum supported weight. Remarkably, the equilibrium height at the maximum supported weight is $\tilde{h}_{\mathrm{eq}}(\tilde{W}_{\max}) \simeq 0.3\tilde{H}_{\mathrm{bv}}$ for $\alpha \gg 1$, which is also true with a similar prefactor for $\alpha \ll 1$ (figure 2*b*), so that the following holds over the range $0 < \alpha \leqslant 100$:

$$\tilde{h}_{\mathrm{eq}}(\tilde{W}_{\max}) \approx 0.3\tilde{H}_{\mathrm{bv}}. \tag{3.6}$$

While it is not straightforward to rationalize the linear relation between h_{eq} and $\mathcal{G}$, we note that $\tilde{B}/\tilde{R}^2 = \tilde{F}_{\mathrm{bv}}/\tilde{H}_{\mathrm{bv}} = \tilde{k}_{\mathrm{bv}}$, with $\tilde{k}_{\mathrm{bv}}$ a natural scale for stiffness, analogous to a spring constant. Then, (3.5*b*) for $\alpha \gg 1$ can be written $\tilde{h}_{\mathrm{eq}} \approx 0.05\tilde{W}/\tilde{k}_{\mathrm{bv}}$.

3.2.3. *Contactless adhesion – Sheet's deformations*

Some of the insights gained from the weak forcing analysis presented in §3.1 carry over to the regime $\alpha \gg 1$. In particular, we show in figure 5 that the excitation of

higher-order modes of deformation as $\mathcal{G} \to 0$, $h_{\rm eq} \to 0$ remains valid. One important difference, however, is the amplitude of the sheet's deformation. In particular, we show in figure 6(a,b) an illustration of the sheet's shape for $\alpha = 20$. For $\mathcal{G} < \mathcal{G}_{\max}$, panel (a), the sheet remains convex, as expected from the large gravitational pull alone. For $\mathcal{G} > \mathcal{G}_{\max}$, panel (b), the sheet becomes concave when the active forcing pulls it away from the wall. This, in turn, causes the sheet's edge to come into contact with the substrate. We confirm in figure 6(c) that turning the sheet concave during part of the vibration cycle is what leads to contact with the wall, and therefore what sets $G_{\max}$. This change in convexity occurs when the active pull is maintained for a sufficiently long time compared to the time it takes for the sheet to undergo a significant change in shape. This process is associated with a timescale $\tilde{T}_g(\tilde{h}_{\rm eq})$, the gravitational timescale defined in (2.9), with $\tilde{h}_{\rm eq} \sim \tilde{W}/\tilde{k}_{bv}$ from (3.5b). Indeed, the static convex shape of the sheet is due to its uniform weight. The criterion for contact is then $\tilde{\omega}\tilde{T}_g(\tilde{h}_{\rm eq}) \sim (\tilde{F}_{\rm bv}/\tilde{W})^3 \lesssim 1$, and we recover the scaling (3.4) for the maximum supported weight for $\alpha \gg 1$, i.e., $\tilde{W}_{\max} \sim \tilde{F}_{\rm bv}$. We note that this understanding relies heavily on the convexity of the sheet and, consequently, on the specific distribution of weight and of active force. While we have assumed a uniform weight distribution, the effects of non-uniform weight distribution remain to be explored.

3.2.4. *Adhesion with contact*

For $\alpha \gtrsim 9$ and sufficiently large $\mathcal{G}$, we observe in figure 4(b,c) that adhesion can be maintained while the sheet's edges come in periodic contact with the substrate. The dynamics in this regime is illustrated in figure 6. To handle contact numerically, we have introduced the repulsive potential $f_w(h)$ in (2.6), which models an elastic collision. Although numerical simulations can access the contact regime, contact introduces additional physical effects beyond the scope of the present model. This regime is therefore not examined further in this article. Nonetheless, we want to point to a possible analogy with suction cups (Ramanarayanan 2024), which achieve strong adhesion through edge contact and pressure differentials. Suction cups are prone to failure, with small perturbations at their edges leading to detachment (Tiwari & Persson 2019). It has been demonstrated that applying vibrations to suction cups improves their performance and reliability (Zhu *et al.* 2006; Wu *et al.* 2023), an idea that shares similarities with the contact regime of vibrated sheets described above. An experimental confirmation of this regime would be valuable and could guide further investigations into its modelling and underlying dynamics.

4. Inertial effects: influence of the Reynolds number

We now introduce the effects of a finite Reynolds number $\mathrm{Re}_{\rm bv} = \tilde{\rho}_a\tilde{\omega}\tilde{R}^4/\tilde{B} > 0$ as defined in (2.3) in the dynamics of adhesion, for an incompressible fluid ($\mathrm{Sq}_{\rm bv} = 0$) and an inertialess sheet ($\mathcal{I}_{\rm bv} = 0$). The governing equations are then (2.4) with $\rho = 1$, (2.5) which corrects the lubrication equations to account for fluid inertia as discussed previously, and the force balance (2.6). Using the parameter values described in §2, $\mathrm{Re}_{\rm bv} = \mathcal{O}(10^4)$. We will see that the actual effects of fluid inertia are, in fact, more properly characterised by $\mathrm{Re}_{\rm eq} = h_{\rm eq}^2\mathrm{Re}_{\rm bv} \lesssim \mathcal{O}(10)$, the Reynolds number that uses the equilibrium height as the characteristic length. Further, $\mathrm{Re}_{\rm bv}$ depends strongly on the details of the experiment (vibration frequency, sheet's radius, and bending modulus), and both the regimes of small and large $\mathrm{Re}_{\rm bv}$ can be relevant depending on the system's scale.

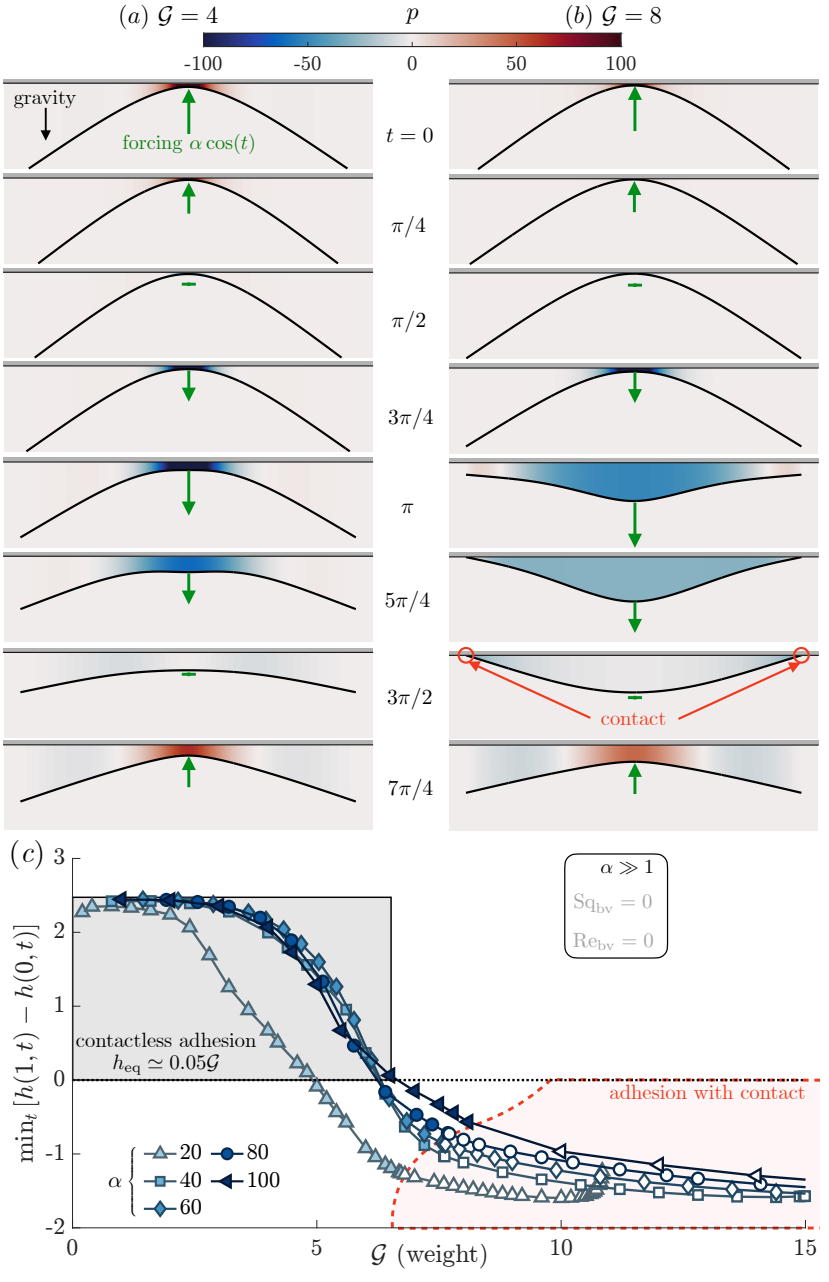

Figure 6: (a, b) Sheet's shape and pressure field over a period of vibration for $\alpha = 20$ and (a) $\mathcal{G} = 4$, (b) $\mathcal{G} = 8$. The green arrows represent the active force schematically, periodically pushing and pulling at the centre of the sheet. In (b), at $t = 3\pi/2$, the edges of the sheet touch the bottom wall. (c) The difference in height between the sheet's center $h(0,t)$ and its edge $h(1,t)$ is a measure of the sheet's convexity: when $\min_t(h(x = 1,t) - h(x = 0,t)) > 0$, the sheet always remain convex as in panel (a), and the linear relationship $h_{\mathrm{eq}} \simeq 0.05\mathcal{G}$ between equilibrium height and weight is verified for $\alpha \gg 1$ (see figure 4*b*). The existence of a concave part during the vibration cycle, as shown at $t = \pi$, $5\pi/4$ and $3\pi/2$ in panel (b), is associated with contact with the wall for $\alpha \gg 1$. Filled symbols represent the case when the sheet never touches the wall, open symbols correspond to the sheet periodically touching the wall.

4.1. *Rigid sheets*

To qualitatively understand the effect of fluid inertia, we begin with an idealised, simplified setup: a standard squeeze film where the gap between the wall and a rigid sheet oscillates harmonically. We consider the flow in the gap and project the Navier-Stokes momentum equations along a streamline:

$$\tilde{\rho}\left(\frac{\partial \tilde{v}_s}{\partial \tilde{t}} + \tilde{v}_s \frac{\partial \tilde{v}_s}{\partial \tilde{s}}\right) = -\frac{\partial \tilde{p}}{\partial \tilde{s}} + \tilde{\mu}\tilde{\nabla}^2 \tilde{v}_s, \tag{4.1}$$

where $\tilde{s}$ and $\tilde{v}_s$ refer to the position and velocity along the streamline, respectively. We integrate this equation along a streamline whose ends are at the top of the sheet, close to $x = 0$, and within the gap at a position $\tilde{s}$, as shown in figure figure 7(a), to find an energy balance analogous to Bernoulli's principle:

$$\left(\tilde{p}\big|_{\tilde{s}=0} + \frac{1}{2}\tilde{\rho}\tilde{v}_s^2\big|_{\tilde{s}=0}\right) - \left(\tilde{p}\big|_{\tilde{s}} + \frac{1}{2}\tilde{\rho}\tilde{v}_s^2\big|_{\tilde{s}}\right) + \int_0^{\tilde{s}} \tilde{\rho}\frac{\partial \tilde{v}_s}{\partial \tilde{t}}\bigg|_{\tilde{s}'} \mathrm{d}\tilde{s}' = \Delta\tilde{p}_{\mathrm{visc}}, \tag{4.2}$$

with $\Delta\tilde{p}_{\mathrm{visc}} = \int_0^{\tilde{s}} \tilde{\mu}\tilde{\nabla}^2\tilde{v}_s \, \mathrm{d}\tilde{s}'$ the pressure loss due to viscous stresses. According to lubrication scalings: $\tilde{v}_s\big|_{\tilde{s}=0} = \dot{\tilde{h}} \ll \tilde{v}_s\big|_{\tilde{s}} \simeq -\dot{\tilde{h}}\tilde{x}/\tilde{h}$, with overdots denoting time derivatives. We use $\tilde{s} \simeq \tilde{x}$ away from $\tilde{s} = 0$ since the flow in the gap is predominantly horizontal under the lubrication approximation. Then, in terms of scaling, $\int_0^{\tilde{s}}(\partial\tilde{v}_s/\partial\tilde{t})\mathrm{d}\tilde{s}' \sim [(\dot{\tilde{h}})^2 - \ddot{\tilde{h}}/\tilde{h}]\,\tilde{x}^2$ and $\Delta\tilde{p}_{\mathrm{visc}} \sim -\tilde{\mu}\dot{\tilde{h}}\tilde{x}^2/\tilde{h}^3$. Equation (4.2) together with these scaling, gives the following pressure profile: $\tilde{p}(\tilde{x},\tilde{t}) \sim (\tilde{R}^2 - \tilde{x}^2)[-\tilde{\mu}\dot{\tilde{h}}/\tilde{h}^3 - \tilde{\rho}\ddot{\tilde{h}}/\tilde{h} + \tilde{\rho}\dot{\tilde{h}}^2/\tilde{h}^2]$, with prefactors missing in front of each term representing, respectively, viscous effects, unsteady inertia, and convective inertia. The formal inertial lubrication analysis from (2.5) leads to the following, in dimensionless form:

$$p(x,t) = \left(1 - x^2\right)\left(-6\frac{\dot{h}}{h^3} - \frac{3\mathrm{Re}}{5}\frac{\ddot{h}}{h} + \frac{51\mathrm{Re}}{35}\frac{\dot{h}^2}{h^2}\right) + p(x=1,t), \tag{4.3}$$

with $p(x=1,t)$ the pressure at the edge found from the boundary condition (2.11), $\mathrm{Re} = \tilde{\rho}_a\tilde{\omega}\tilde{h}_0^2/\tilde{\mu}$, and $\tilde{h}_0$ the typical oscillation height. The first term describes the viscous losses and is captured by standard lubrication theory. The unsteady acceleration term, proportional to $-\ddot{h}/h$, is equivalent to an added mass effect as discussed below. The edge pressure tends to decrease the pressure in the gap; however, the dominant effect of inertia is to convert the kinetic energy density of the fluid drawn into (or ejected from) the gap into pressure. This is illustrated in figure 7 where a squeeze flow is imposed by setting the height as $h(t) = 1 + a\cos(t)$, $0 < a < 1$. We show both the pressure profile and velocity vectors in panels (c) and (d) for the purely viscous analysis and the inertial corrections, respectively. Over one period of oscillations, the net normal force from viscous effects cancels out, as expected: $\int_{-1}^{1}\langle p_{\mathrm{viscous}}(x,t)\rangle \, \mathrm{d}x = 0$, with $p_{\mathrm{viscous}}(x,t) = -6\left(1-x^2\right)\dot{h}(t)/h^3(t)$. However, the force from inertial effects is positive, $\int_{-1}^{1}\langle p_{\mathrm{inertial}}(x)\rangle \, \mathrm{d}x = (1 - 7k/24)a^2\mathrm{Re}/1.5 + \mathcal{O}(a^4) > 0$, with $p_{\mathrm{inertial}} = p - p_{\mathrm{viscous}}$ and $k = 0.5$ a loss coefficient introduced in the boundary condition (2.11), showing that inertia leads to a normal force that pushes the sheet away from the wall. This effect has long been known in the context of bearings (e.g., Kuzma (1968); Tichy & Winer (1970); Jones & Wilson (1975)). In addition to modifying the pressure, a non-zero Reynolds number also alters the

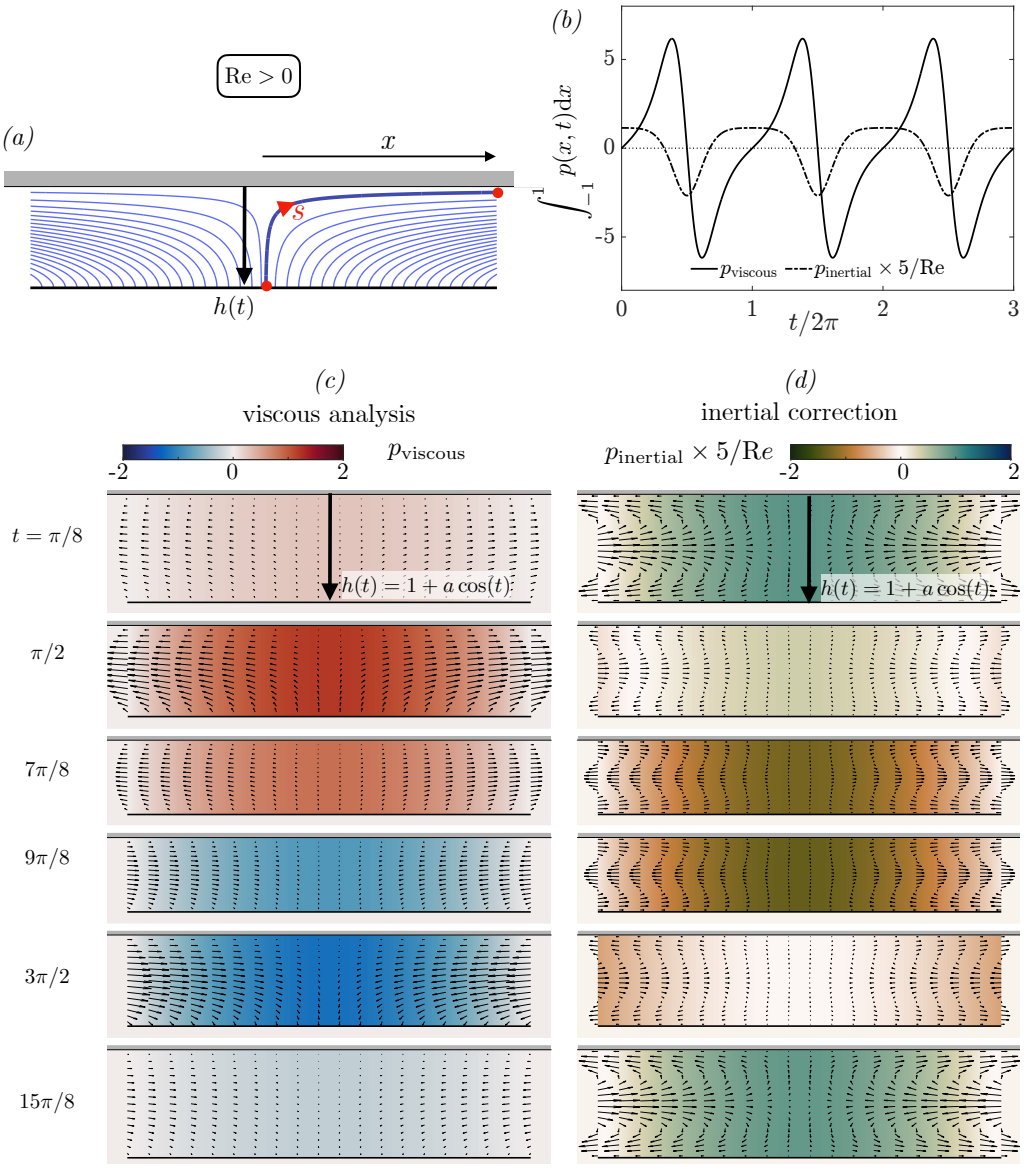

Figure 7: Squeeze flow of a rigid plate moving normal to a wall with a height evolving as $h(t) = 1 + a\cos(t)$, shown for illustration here with $a = 0.4$. The pressure is computed from (4.3) and the fluid velocity from the calculations carried out in appendix A. (*a*) Streamlines of the flow associated with a rigid sheet moving towards a wall or away from it. (*b*) Integral of pressure in space for the viscous component and inertial component. Integrated in time, the viscous component averages to zero while the inertial component gives a positive force. The inertial pressure is rescaled by the Reynolds number. (*c, d*) Velocity profiles (arrows) and pressure field (colours) isolating (*c*) the dominant viscous flow and (*d*) the inertial corrections.

parabolic velocity profile predicted by the purely viscous theory: the horizontal velocity profile becomes a 6^{th}-order polynomial which allows for secondary flows (figure 7*c*), a common feature of pulsatile flows (Womersley 1955). We finally note that the unsteady acceleration term, proportional to $\ddot{h}$, appears as a height-dependent added mass. Indeed, integrating the pressure over the sheet's length $2\tilde{R}$ gives rise to a force per unit length $-\tilde{m}_a\dddot{\tilde{h}}$, with $\tilde{m}_a = 4\tilde{\rho}\tilde{R}^3/5\tilde{h}$ that can be interpreted as an added mass per unit length (see also (D 5)). In contrast, the added mass of a plate far from any boundary is proportional to $\tilde{\rho}\tilde{R}^2$ (Brennen 1982).

While we initially considered a sheet constrained in position for simplicity, we are more interested in the case of a weightless rigid sheet driven periodically by a dimensionless force $\alpha\cos(t)$. In this case, a two-timescale asymptotic analysis can be used to find the evolution of the height $h(t)$ in the asymptotic limit $\alpha^2\mathrm{Re} \ll 1$. We present the derivation in appendix D, where we show that the sheet slowly moves away from the wall to accommodate the increase in pressure due to inertia while maintaining a force balance. The sheet's time-averaged position has the following evolution equation, in dimensionless and dimensional form:

$$\frac{1}{\alpha^2\langle h\rangle^2}\frac{\mathrm{d}\langle h\rangle}{\mathrm{d}t} = c_k\mathrm{Re}\langle h\rangle^5, \quad \frac{\mathrm{d}\langle\tilde{h}\rangle}{\mathrm{d}\tilde{t}} = c_k\frac{\tilde{F}_a^2\tilde{\rho}_a\langle\tilde{h}\rangle^7}{\tilde{\mu}^3\tilde{R}^8} = \frac{c_k\langle\tilde{h}\rangle}{\tilde{T}_{\mathrm{a,i}}\Big(\langle\tilde{h}_0\rangle\Big)}, \quad c_k = \frac{1-\frac{7k}{16}}{224} \tag{4.4}$$

which indeed shows repulsion from the wall, $\mathrm{d}\langle h\rangle/\mathrm{d}t > 0$. The fact that $\mathrm{d}(\langle h\rangle)/\mathrm{d}t \sim \langle h\rangle^7$ – a much stronger dependence on $\langle h\rangle$ than the effects of gravity and elastohydrodynamic, which show respectively $\mathrm{d}(\langle h\rangle)/\mathrm{d}t \sim h^3$ and h^2 as shown in (3.2) – follows from the expressions of the relevant timescales discussed in §2.4. In particular, the inertial timescale shows the strongest dependence on the height, $\tilde{T}_{a,i}(\tilde{h}) \sim \tilde{h}^{-6}$. We also note that the boundary condition (2.11) appears in the prefactor c_k and leads to a correction of the order of $7k/16 \simeq 22\%$ for $k = 0.5$ as compared to the standard boundary condition $p = 0$.

4.2. *Soft sheets*

We expect that the destabilising influence of fluid inertia observed in rigid systems qualitatively extends to soft sheets, weakening the viscous adhesion mechanism discussed in the previous section. We solve the governing equations for soft sheets with $\mathrm{Sq}_{\mathrm{bv}} = I_{\mathrm{bv}} = 0$ and for $\alpha = 1$ and $\alpha = 20$, corresponding to the regimes of weak and strong forcing, respectively. For both values, we systematically studied the relationship between the equilibrium height h_{eq} and the weight $\mathcal{G}$, as well as the maximum supported weight $\mathcal{G}_{\max}$, as a function of the Reynolds number $\mathrm{Re}_{\mathrm{bv}}$. As we discussed in §2.7, for each set of parameters we define the equilibrium Reynolds number $\mathrm{Re}_{\mathrm{eq}} = h_{\mathrm{eq}}^2\mathrm{Re}_{\mathrm{bv}}$ that is based on the actual equilibrium height rather than on the heightscale $\tilde{H}_{\mathrm{bv}}$ and which is representative of the actual magnitude of inertial over viscous effects; hence, $\mathrm{Re}_{\mathrm{eq}}$ may be small even when $\mathrm{Re}_{\mathrm{bv}}$ is large.

Figure 8 summarizes our results for $\alpha = 1$. There, we show examples of bifurcation diagrams and the associated regime map of reachable weights as a function of $\mathrm{Re}_{\mathrm{bv}}$. For small values of $\mathrm{Re}_{\mathrm{bv}}$, increasing the Reynolds number first marginally increases the maximum weight $\mathcal{G}_{\max}$, up to $\mathcal{G}_{\max} \simeq 0.15$ for $\mathrm{Re}_{\mathrm{bv}} \simeq 40$, to be compared with $\mathcal{G}_{\max} \simeq 0.14$ for $\mathrm{Re}_{\mathrm{bv}} = 0$. Further increasing $\mathrm{Re}_{\mathrm{bv}}$ then leads to a sharp decrease in $\mathcal{G}_{\max}$, explained by the destabilising effect of fluid inertia discussed previously. Figure 8(*d*) shows the range of accessible equilibrium Reynolds numbers $\mathrm{Re}_{\mathrm{eq}}$ as a function of $\mathrm{Re}_{\mathrm{bv}}$. This demonstrates that $\mathrm{Re}_{\mathrm{bv}}$ has little effect on the dynamics as

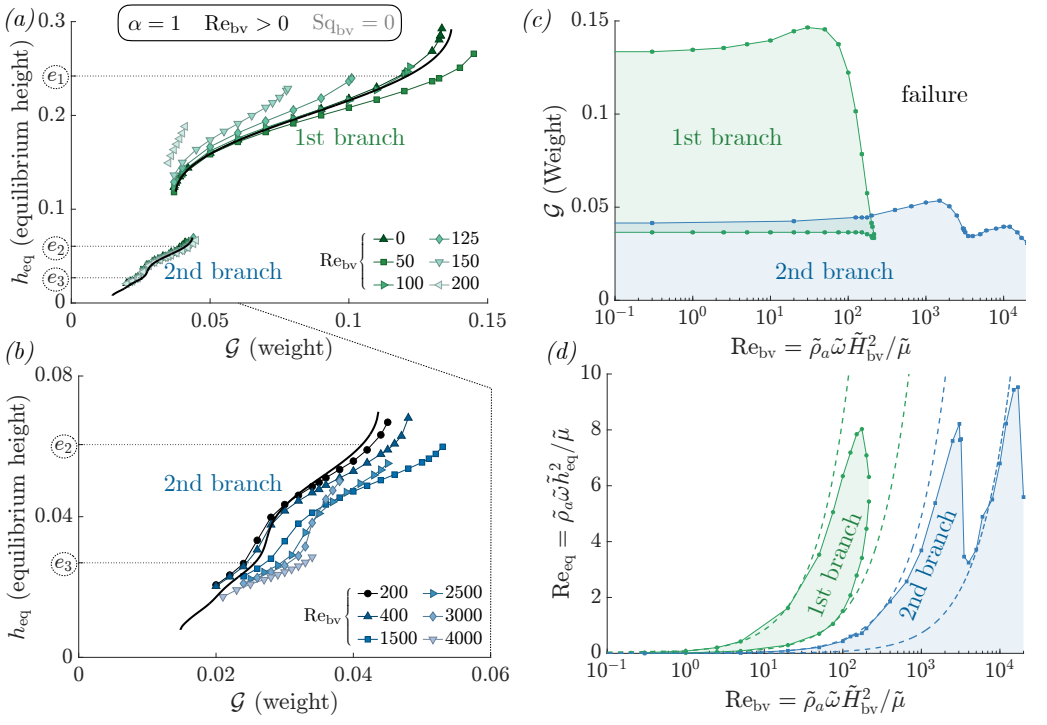

Figure 8: (a–b) Equilibrium height as a function of the dimensionless weight with $\mathrm{Sq_{bv}} = \mathcal{I}_{\mathrm{bv}} = 0$ and $\alpha = 1$ for (a) $\mathrm{Re_{bv}} < 200$ and (b) $\mathrm{Re_{bv}} > 200$. Black lines are the stable equilibria of (3.2). (c) Phase diagram showing the accessible weights as a function of $\mathrm{Re_{bv}}$. The first equilibrium branch corresponds to $h_{\mathrm{eq}} > 0.1$, the second branch to $h_{\mathrm{eq}} < 0.1$. (d) Reynolds number based on the equilibrium height h_{eq}, $\mathrm{Re_{eq}} = h_{\mathrm{eq}}^2 \mathrm{Re_{bv}}$ as a function of the control parameter $\mathrm{Re_{bv}}$. The dashed lines represent cases where h_{eq} is constant and illustrate the expected behaviour if fluid inertia did not affect the system.

long as $\mathrm{Re_{eq}} \lesssim 1$. Beyond this, once $\mathrm{Re_{eq}} = \mathcal{O}(1)$, $\mathcal{G}_{\max}$ decreases together with h_{eq} to ensure $\mathrm{Re_{eq}}$ remains relatively small. In particular, we observe a sharp drop in $\mathcal{G}_{\max}$ for $\mathrm{Re_{bv}} \gtrsim 30 \approx 1/e_1^2$. As $\mathrm{Re_{bv}}$ keeps increasing, the first branch of the bifurcation diagram (continuous black line for $h_{\mathrm{eq}} > 0.1$ in figure 8a) is eventually not accessible anymore for $\mathrm{Re_{bv}} \gtrsim 200 \approx 1/e_2^2$. We observe a similar drop of $\mathcal{G}_{\max}$ for $\mathrm{Re_{bv}} \approx 2000 \approx 1/e_3^2$, as the first part of the second equilibrium branch (corresponding to the excitation of the second eigenmode ζ_2 for $h_{\mathrm{eq}} \approx e_2$) is also no longer accessible.

The system's behavior is qualitatively similar in the regime of strong forcing, as illustrated in figure 9 for $\alpha = 20$: the maximum supported weight decreases as $\mathrm{Re_{bv}}$ increases, with sharp drops at specific Reynolds numbers, while the equilibrium height shows minor variations with $\mathrm{Re_{bv}}$. Similarly to the weak forcing case, these drops are associated with higher-order modes as illustrated in panel (b). An important difference between the weak and strong forcing regimes is that the equilibrium Reynolds number $\mathrm{Re_{eq}}$ can become relatively large in the latter, and we observe values up to $\mathrm{Re_{eq}} = \mathcal{O}(10^2)$ for $\mathrm{Re_{bv}} = \mathcal{O}(10^4)$. For such large values, the first-order inertial corrections to lubrication theory (eq. (2.5) and appendix A) may no longer be valid, and higher-order corrections, or full Navier-Stokes simulations, may be necessary to accurately describe the flow and $\mathcal{G}_{\max}$. The experiments of Weston-Dawkes *et al.* (2021) suggest that the regime $\mathrm{Re_{eq}} = \mathcal{O}(10 - 100)$ is relevant

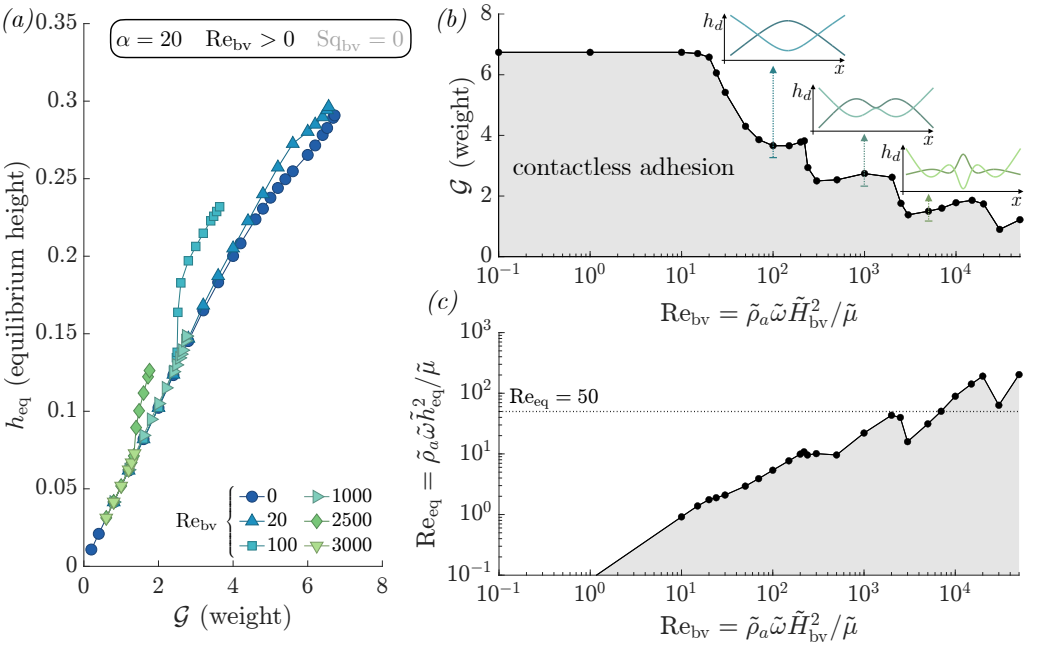

Figure 9: Effect of the fluid inertia with $\mathrm{Sq_{bv}} = \mathcal{I}_{\mathrm{bv}} = 0$ and $\mathrm{Re_{bv}} > 0$ for $\alpha = 20$. (a) Equilibrium height as a function of the dimensionless weight for the regime of contactless adhesion. (b) Regime maps and the associated (c) range of Reynolds number based on equilibrium height $\mathrm{Re_{eq}}$. The inertial lubrication theory is not expected to be valid for $\mathrm{Re_{eq}} \gtrsim 50$. In ($b$), we show illustrations of h_d (as defined in (3.3)) for $\mathrm{Re_{bv}}$=10, 1000 and 5000 at $t = \pi/2$ and $3\pi/2$.

experimentally. We also make an anecdotal observation that for $200 < \mathrm{Re}_{bv} < 300$ the sheet can respond at half the forcing frequency without altering the adhesion strength. Such period doubling is a well-known feature of nonlinear forced systems, and has been observed and predicted in inertial lubrication flows with free surfaces (Rojas *et al.* 2010).

5. Compressible effects: influence of the Squeeze number

In this section, we neglect inertia ($\mathcal{I}_{\mathrm{bv}} = \mathrm{Re_{bv}} = 0$) and study the influence of the fluid's compressibility, $\mathrm{Sq_{bv}} > 0$, assuming that it behaves as an isothermal ideal gas. We assume that the two bounding surfaces, the rigid wall and the elastic sheet, are isothermal, and the characteristic timescale for temperature variations within the thickness of the gap is then $\tilde{H}^2_{\mathrm{bv}}/\tilde{D}$ with $\tilde{D}$ the thermal diffusivity of the gas. Comparing this time with the characteristic forcing time $\tilde{\omega}^{-1}$ defines a Péclet number $\mathrm{Pe} = \tilde{\omega}\tilde{H}^2_{\mathrm{bv}}/\tilde{D}_{\mathrm{th}} = \mathrm{Re_{bv}Pr}$ with $\mathrm{Pr} = \tilde{\mu}/\tilde{\rho}_a\tilde{D}_{\mathrm{th}} \simeq 0.7$ the Prandtl number. Our assumption of isothermal gas is appropriate for small Pe and therefore for small Reynolds numbers. We make this assumption and therefore use the isothermal ideal gas law (2.4b). In the opposite limit of an isentropic gas, valid for large Péclet numbers, the pressure-density relation would become: $\tilde{\rho}/\tilde{\rho}_a = (1 + \tilde{p}/\tilde{p}_a)^{1/\gamma}$ with γ the adiabatic index ($\gamma \simeq 1.4$ for air (Haynes 2016)), or in dimensionless units $\rho = (1 + \mathrm{Sq_{bv}}p)^{1/\gamma}$. The essential mechanism of increase in density with increasing pressure would still be valid, such that the results discussed next would

be qualitatively similar; in particular, for small $\mathrm{Sq_{bv}}$ the first-order Taylor expansion of the isentropic relation is $\rho = 1 + \mathrm{Sq_{bv}} p/\gamma$, identical to the isothermal one (2.4*b*) up to a prefactor in $\mathrm{Sq_{bv}}$.

5.1. *Rigid sheets*

To build intuition, we first consider the squeeze film setup with a rigid: $\tilde{h} = \tilde{h}_0(1 + a\cos(\tilde{\omega}\tilde{t}))$. As discussed in §2, the effects of compressibility are quantified with the Squeeze number $\mathrm{Sq} = \tilde{\mu}\tilde{\omega}\tilde{R}^2/\tilde{h}_0^2\tilde{p}_a$, which compares the viscous stresses to the ambient pressure $\tilde{p}_a$. When the sheet approaches the wall, a competition arises between the outflow of fluid from the gap, resisted by viscosity, and the compression of the fluid, resisted by its bulk modulus. For an isothermal ideal gas, the bulk modulus is the pressure. For $\mathrm{Sq} \ll 1$, the resistance to compression is much weaker than the resistance to flow, and an incompressible description is appropriate. Conversely, for $\mathrm{Sq} \gg 1$, viscous stresses become so large that there is almost no outflow, and the fluid is compressed similarly to a piston. Likewise, fluid is expanded when the surface moves away from the wall. In this limit $\mathrm{Sq} \gg 1$, also examined by Salbu (1964) to gain physical insights, the work per unit area to expand from $\tilde{h}_0$ to $\tilde{h}_0(1+a)$ is $\tilde{w}_{+a} = \int_{\tilde{h}_0}^{\tilde{h}_0(1+a)} \tilde{p}\mathrm{d}\tilde{h} = \tilde{p}_a\tilde{h}_0\ln(1+a)$, and the work to compress from $\tilde{h}_0$ to $\tilde{h}_0(1-a)$ is $\tilde{w}_{-a} = \tilde{p}_a\tilde{h}_0\ln(1-a)$, where we have used $\tilde{p}\tilde{h} = \tilde{p}_a\tilde{h}_0$ from the isothermal ideal gas law. This gives $|\tilde{w}_{-a}| - |\tilde{w}_{+a}| = -\tilde{p}_a\tilde{h}_0\ln(1-a^2) = \tilde{p}_a\tilde{h}_0\tilde{a}^2 + \mathcal{O}(a^4) > 0$, i.e., it is more energetically costly to compress than to expand an ideal gas by the same volume increment. This is simply due to the fact that the isothermal bulk modulus of the gas is its pressure, which increases during compression and decreases during expansion.

We now come back to the original setting, the displacement of the rigid sheet not constrained, but controlled by a time-periodic force $\alpha\cos(t)$. The same magnitude of force applies when compressing and expanding periodically, and we can anticipate that at each cycle, there will be more expansion than compression, i.e., the sheet will slowly move away from the wall. An asymptotic expansion performed in Appendix E shows that the sheet's time averaged position follows at $\mathcal{O}(\alpha^2\mathrm{S_q})$, in dimensional and dimensionless form:

$$\frac{1}{\alpha^2\langle h\rangle^2}\frac{\mathrm{d}\langle h\rangle}{\mathrm{d}t} = \frac{3}{8}\mathrm{Sq_{bv}}\langle h\rangle, \quad \frac{\mathrm{d}\langle\tilde{h}\rangle}{\mathrm{d}\tilde{t}} = \frac{3}{8}\frac{\tilde{F}_a^2\langle\tilde{h}\rangle^3}{\tilde{\mu}\tilde{R}^6\tilde{p}_a} = \frac{3}{8}\frac{\langle\tilde{h}\rangle}{\tilde{T}_{\mathrm{a,c}}\left(\langle\tilde{h}\rangle\right)}. \tag{5.1}$$

We can compare (5.1) to (3.2), where the isolated effect of gravity on a rigid sheet leads to $\mathrm{d}\langle h\rangle/\mathrm{d}t = \mathcal{G}\langle h\rangle^3/4$. The fact that these two very different physical processes lead to the same scaling $\mathrm{d}\langle h\rangle/\mathrm{d}t \sim \langle h\rangle^3$ originate from the definition of the compressible timescale $\tilde{T}_{\mathrm{a,c}}$ and gravitational timescale $\tilde{T}_g$ in (2.9). This shows that the first-order effect of compressibility can be interpreted as an increase in the effective dimensionless weight $\mathcal{G}_{\mathrm{eff}}$ (or dimensional weight $\tilde{W}_{\mathrm{eff}}$) such that:

$$\mathcal{G}_{\mathrm{eff}} = \mathcal{G} + \frac{3}{2}\alpha^2\mathrm{Sq_{bv}}, \quad \tilde{W}_{\mathrm{eff}} = \tilde{W} + \frac{3}{2}\frac{\tilde{F}_a^2}{\tilde{p}_a\tilde{R}^2}. \tag{5.2}$$

While we focus on small Squeeze numbers, we note for completeness that the averaged normal force acting on a sheet subject to a squeeze film motion can be approximated analytically for arbitrary values of $\mathrm{Sq_{bv}}$ (Taylor & Saffman 1957; Langlois 1962).

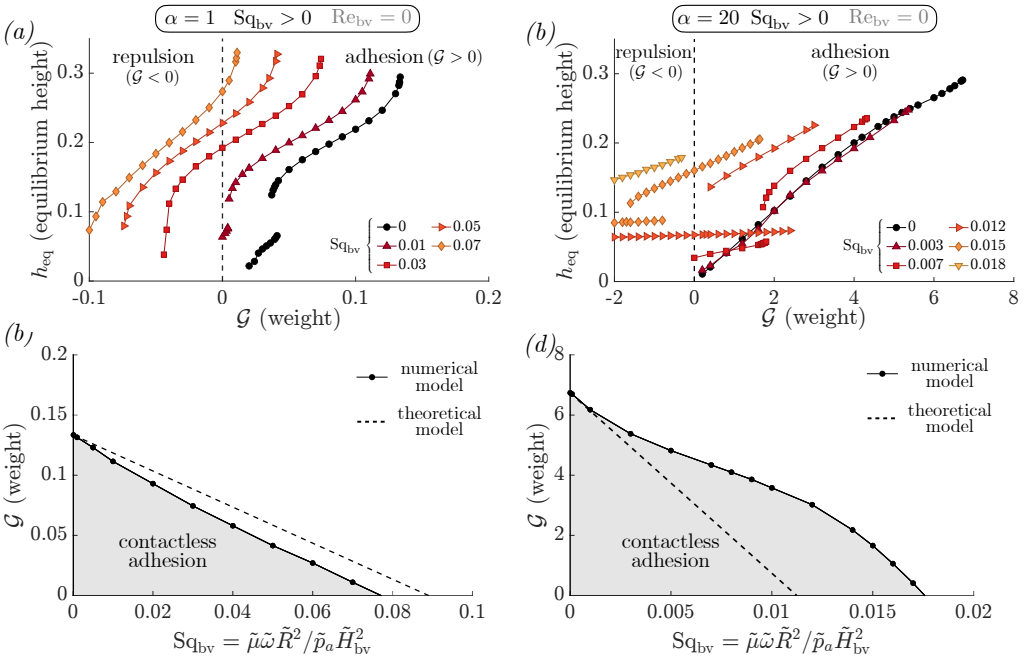

Figure 10: $(a-b)$ Effect of the fluid compressibility for $\mathrm{Re_{bv}} = \mathcal{I}_{bv} = 0$ and $\mathrm{Sq_{bv}} > 0$. (a,b) correspond to the weak forcing regime with $\alpha = 1$ and (c,d) to the strong forcing regime with $\alpha = 20$. The dashed lines in (b) and (d) are derived from (5.2) and show $\mathcal{G}_{max}(\mathrm{Sq_{bv}}) = \mathcal{G}_{max}(\mathrm{Sq_{bv}} = 0) - 1.5\alpha^2\mathrm{Sq_{bv}}$. We primarily captured the first equilibrium branch and did not systematically investigate the entire extent of the bifurcation diagram.

5.2. *Soft sheets*

We solve the governing equations (2.4), (2.5) and (2.6) with boundary conditions (2.10) and (2.11) in the inertialess limit ($\mathrm{Re_{bv}} = \mathcal{I}_{bv} = 0$); in this case the pressure boundary condition (2.11) reduces to $p = 0$. Our results for the weak forcing regime, $\alpha = 1$, are shown in figure 10(a,b). The results are consistent with (5.2), and the main effect of compressibility is indeed to modify the effective weight with a relation close to (5.2). As compressibility translates the bifurcation diagrams to lower weights, we observe the possibility of reaching an equilibrium height $h_{eq} > 0$ for $\mathcal{G} < 0$, corresponding to gravity pointing towards the wall. In these cases, the repulsive effect of compressibility can balance the adhesive effects of both elastohydrodynamics and gravity. This is reminiscent of near-field acoustic levitation (Shi *et al.* 2019) where objects can levitate above rapidly vibrating surfaces.

We observe similar results in figure 10(c,d) for the strong forcing regime with $\alpha = 20$. The relation (5.2) predicts $\mathcal{G}_{max}$ accurately up to $\mathrm{Sq_{bv}} \approx 10^{-3}$, but underestimates the effective weight by up to 50% at larger squeeze numbers, likely because of the interactions between elastic deformations and compressibility neglected by this simple model. The effects on the equilibrium curves are also more complex than a simple shift of the bifurcation diagram to lower values of weight; in particular, we observe the possibility of hysteresis, similar to the weak forcing regime $\alpha \lesssim 1$ (figure 2b).

6. Discussion and conclusion

We have investigated numerically the elastohydrodynamic adhesion of elastic sheets vibrating near a rigid substrate. Our analysis extends our previous work (Poulain *et al.* 2025) by systematically exploring the regime beyond the weak-forcing limit and by incorporating the first-order corrections of fluid inertia and fluid compressibility into the viscous lubrication dynamics. By using a combination of asymptotic analysis and numerical simulations, we have characterised the conditions under which contactless adhesion or hovering can be maintained.

The described viscous elastohydrodynamic adhesion mechanism exhibits two regimes depending on the relative strength of the forcing, $\alpha = \tilde{F}_a/\tilde{F}_{\mathrm{bv}}$ with $\tilde{F}_a$ the forcing amplitude and $\tilde{F}_{\mathrm{bv}} = (\tilde{\mu}\tilde{\omega}\tilde{B}^2)^{1/3}$ the elastohydrodynamic force scale involving both bending and viscous effects. For weak forcings ($\alpha \lesssim 1$), the full dynamics can be treated analytically using asymptotic analysis, and the maximum supported weight scales as $\tilde{W}_{\max} \sim \tilde{F}_a^2/\tilde{F}_{\mathrm{bv}}$. As the forcing strength increases, the maximum supported weight saturates, and our simulations show $\tilde{W}_{\max} \sim \tilde{F}_{\mathrm{bv}}$ for $\alpha \gg 1$. In both cases, the adhesion height scales as $\tilde{h}_{\mathrm{eq}} \sim \tilde{H}_{\mathrm{bv}} = \tilde{R}^2(\tilde{\mu}\tilde{\omega}/\tilde{B})^{1/3}$ and the sheets respond with higher-order modes of deformation as both the weight and adhesion height decrease.

In the strong forcing limit, we have identified a transition from contactless adhesion to a regime where the sheet's edges periodically come into contact with the substrate. While the present model captures this transition numerically, a complete description of the physics of contact would require additional modelling of the sheet–substrate interactions, and physical effects at a very small scale may additionally impact the dynamics. We also expect that the precise weight distribution, assumed uniform in this work, would influence not only contact but the overall hovering dynamics. Studying the effect of a non-uniform weight or of an external pulling force would thus be a natural extension enabling more direct quantitative comparison with experiments.

In addition to the viscous elastohydrodynamics, we have analysed the role of fluid inertia in this lubrication flow by accounting for finite Reynolds numbers $\mathrm{Re}_{\mathrm{bv}} = \tilde{\rho}_a\tilde{R}^2\tilde{\omega}^2/\tilde{F}_{\mathrm{bv}}$. We have quantified how the Bernoulli-like increase of pressure due to the stagnation point in the thin gap leads to an overall destabilising effect. This effect decreases the maximum supported weight such that the Reynolds number based on the equilibrium height, $\mathrm{Re}_{\mathrm{eq}} = \tilde{\rho}_a\tilde{\omega}\tilde{h}_{\mathrm{eq}}^2/\tilde{\mu} = \mathrm{Re}_{\mathrm{bv}}(\tilde{h}_{\mathrm{eq}}/\tilde{H}_{\mathrm{bv}})^2$, remains relatively small. In particular, we predict that the sheet cannot respond solely through the first-order mode of bending deformations and that higher-order deformation modes must be excited in these experiments; a prediction that can be tested experimentally. While fluid inertia is expected to influence elastohydrodynamic adhesion significantly, our current understanding of its contribution remains qualitative. A more detailed analysis of the fluid–structure coupling at intermediate Reynolds numbers would be valuable for future work and directly relevant to experiments. Indeed, Weston-Dawkes *et al.* (2021) report heights such that $\mathrm{Re}_{\mathrm{eq}} = \mathcal{O}(10-100)$. The range of validity of inertial corrections to lubrication theory for deformable geometries at finite Reynolds numbers, as well as the choice of appropriate boundary conditions, remains an open question.

Moreover, we considered the influence of fluid compressibility for small values of the Squeeze number $\mathrm{Sq}_{\mathrm{bv}} = (\tilde{\mu}\tilde{\omega}\tilde{B}^2)^{1/3}/\tilde{p}_a\tilde{R}^2$ and find that compressibility corrections can be interpreted as an effective weight, which modifies the adhesion threshold predicted by the incompressible analysis. This destabilising effect remains modest

under typical experimental conditions, and our analysis suggests that compressibility is unlikely to play a significant role in the experiments of Weston-Dawkes *et al.* (2021) and Colasante (2016), in contrast to previous predictions (Ramanarayanan *et al.* 2022; Ramanarayanan & Sánchez 2022).

The present model relies on several simplifying assumptions. In particular, it treats the deformation of the sheets as pure bending. While we do not expect qualitatively different behaviours between results in one or two dimensions for small deformations (Poulain *et al.* 2025), this neglects any stretching that would be important for large deformations in two dimensions and the associated possibility of non-axisymmetrical deformations when stretching becomes significant. Second, we have neglected solid inertia. In practice however, the dimensionless parameter comparing effects of solid inertia to viscous elastohydrodynamic effects, $\mathcal{I}_{\rm bv} = \tilde{\rho}_s \tilde{e} \tilde{\omega}^2 \tilde{R}^4/\tilde{B} = {\rm Re}_{\rm bv}(\tilde{\rho}_s/\tilde{\rho}_a)\tilde{e}(\tilde{\mu}\tilde{\omega}/\tilde{B})^{1/3}$, can be large and the role of solid inertia, along with possible resonance effects (Ramanarayanan & Sánchez 2024), should be addressed to characterize the system fully.

In conclusion, our model provides a comprehensive framework for understanding viscous elastohydrodynamic adhesion in vibrated elastic systems, suggesting that this mechanism may operate across scales. While our analysis has been motivated by forced centimetric sheets, experimentally shown to support from a few hundred grams to tens of kilograms, the underlying interplay between periodic forcing, elastic deformation, and the nonlinear response of confined viscous flows is general. We anticipate that similar principles could be leveraged in microscale systems: Applications might include tunable adhesion forces in MEMS or novel pick-and-place strategies for small objects as an alternative to standard, rigid inverted near-field acoustic levitation. One natural avenue for future investigation is the effect of surface texture, as experiments have shown that surface roughness can be detrimental to adhesion of (Weston-Dawkes *et al.* 2021) while large cracks are detrimental at larger scales (Ramanarayanan & Sánchez 2024). This remains to be understood, and also raises the question of whether textured surfaces can be used as a means to control adhesion and, possibly, lateral translation. Indeed, the vibrating sheet can translate along the surface when lateral symmetry is broken (Weston-Dawkes *et al.* 2021; Jia *et al.* 2023; Ramanarayanan & Sánchez 2023), either through spatially varying forcing or gradients in material properties such as stiffness. Exploring this dynamics could allow for the design not only of contactless grippers but also of soft vibrating "swimmers" able to hover near surfaces. The predictions and perspectives developed herein will hopefully inspire detailed experimental investigations.

Declaration of Interests

The authors report no conflict of interest.

Acknowledgments

We thank Sami Al-Izzi, Annette Cazaubiel, and Jingbang Liu for insightful discussions.

Funding

S.P. and A.C. acknowledge funding from the Research Council of Norway through project 341989. T.K. acknowledges funding from the European Union's Horizon

2020 research and innovation programme under the Marie Sklodowska-Curie grant agreement No 801133. L.M. acknowledges funding from the Simons Foundation and the Henri Seydoux Fund.

Appendix A. Inertial correction to lubrication theory

In this appendix, we consider no compressible effect and start from the incompressible Navier-Stokes equation:

$$\tilde{\rho}\left(\frac{\partial \tilde{\boldsymbol{v}}}{\partial \tilde{t}} + \tilde{\boldsymbol{v}}\cdot\tilde{\boldsymbol{\nabla}}\tilde{\boldsymbol{v}}\right) = -\tilde{\boldsymbol{\nabla}}\tilde{p} + \tilde{\mu}\tilde{\boldsymbol{\nabla}}^2\tilde{\boldsymbol{v}}, \tag{A 1a}$$

$$\tilde{\boldsymbol{\nabla}}\cdot\tilde{\boldsymbol{v}} = 0. \tag{A 1b}$$

A.1. *Scalings*

We introduce the characteristic horizontal lengthscale $\tilde{R}$ and the vertical lengthscale $\tilde{H}$ representing, respectively, the radius of the sheet and the thickness of the gap. The aspect ratio is $\varepsilon = \tilde{H}/\tilde{R} \ll 1$. We let $\tilde{U}$ be the vertical velocity scale. From mass conservation (A 1*b*), the horizontal velocity scale is $\tilde{U}/\tilde{\varepsilon}$. Following lubrication theory for $\varepsilon \ll 1$, we scale the pressure by realising that the longitudinal pressure gradients induce a flow mainly resisted by transverse viscous stresses (Batchelor 1967), leading to the pressure scale $\tilde{P} = \tilde{\mu}\tilde{U}/(\varepsilon^2\tilde{H})$. We decompose the velocity $\boldsymbol{v} = (\boldsymbol{v}_\perp, v_z)$ into its horizontal and vertical components, and introduce the following dimensionless variables:

$$\begin{gathered} t = \tilde{t}\tilde{\omega}, \quad (x,y) = (\tilde{x},\tilde{y})/\tilde{R}, \quad (z,h) = (\tilde{z},\tilde{h})/\tilde{H}, \\ \boldsymbol{v}_\perp = \varepsilon\tilde{\boldsymbol{v}}_\perp/\tilde{U}, \quad v_z = \tilde{v}_z/\tilde{U}, \quad p = \varepsilon^2\tilde{p}/(\tilde{\mu}\tilde{U}), \quad \rho = \tilde{\rho}/\tilde{\rho}_a. \end{gathered} \tag{A 2}$$

The dimensionless horizontal momentum balance (A 1*a*) is at $\mathcal{O}(\varepsilon^2)$:

$$\mathrm{Wo}^2\frac{\partial \boldsymbol{v}_\perp}{\partial t} + \mathrm{Re}\,(\boldsymbol{v}\cdot\boldsymbol{\nabla})\,\boldsymbol{v}_\perp = -\boldsymbol{\nabla}_\perp p + \frac{\partial^2 \boldsymbol{v}_\perp}{\partial z^2}. \tag{A 3}$$

The Womersley number Wo is defined as $\mathrm{Wo}^2 = \tilde{\rho}_a\tilde{\omega}\tilde{H}^2/\tilde{\mu}$ and characterizes the unsteady inertia, while the Reynolds number $\mathrm{Re} = \tilde{\rho}_a\tilde{V}\tilde{H}/\tilde{\mu}$ characterizes convective inertia. Their ratio defines a Strouhal number $\mathrm{St} = \mathrm{Wo}^2/\mathrm{Re} = \tilde{\omega}\tilde{H}/\tilde{V}$.

We assume that the flow is driven by oscillations or vibrations of typical amplitude $\tilde{a}$ and frequency $\tilde{\omega}$. The vertical speed scale is then $\tilde{V} = \tilde{\omega}\tilde{a}$, so that $\mathrm{St} = \tilde{H}/\tilde{a}$. When $\tilde{a}/\tilde{H} \ll 1$, i.e., when the vibration amplitude is small compared to the thickness of the fluid layer, it may be possible to neglect convective acceleration terms but to include unsteady effects. This leads to the unsteady Stokes equation, which is linear and allows for analytical treatments of oscillatory flows (e.g. Womersley 1955; Fouxon & Leshansky 2018; Fouxon *et al.* 2020; Zhang *et al.* 2023; Bigan *et al.* 2024). In our case, the amplitude of the vibrations is a priori unknown and, as we will see, can be comparable to $\tilde{H}$. We therefore scale it as the gap height itself, letting $\tilde{a} = \tilde{H}$. In this case, $\mathrm{St} = 1$, $\mathrm{Wo}^2 = \mathrm{Re} = \tilde{\rho}_a\omega\tilde{H}^2/\tilde{\mu}$, and include the effects of unsteady and convective inertia at the same asymptotic order $\mathcal{O}(\mathrm{Re})$.

A.2. *Elastohydrodynamic inertial lubrication equations*

e make the assumption St = 1, Re = Wo, and rewrite (A 1) differentiating between the horizontal direction $\boldsymbol{x}_\perp = (x, y)$ and the vertical direction z:

$$\mathrm{R_e}\left(\frac{\partial}{\partial t} + (\boldsymbol{v}\cdot\boldsymbol{\nabla})\right)\boldsymbol{v}_\perp = -\boldsymbol{\nabla}_\perp p + \frac{\partial^2 \boldsymbol{v}_\perp}{\partial z^2} + \mathcal{O}(\varepsilon^2), \tag{A 4a}$$

$$0 = -\frac{\partial p}{\partial z} + \mathcal{O}(\varepsilon^2, \varepsilon^2 \mathrm{R_e}), \tag{A 4b}$$

$$\boldsymbol{\nabla}_\perp \cdot \boldsymbol{v}_\perp + \frac{\partial v_z}{\partial z} = 0. \tag{A 4c}$$

We seek a depth-integrated description of the flow. The momentum balance normal to the wall (A 4*b*) shows that $\tilde{p}$ is independent of $\tilde{z}$. Integrating (A 4*c*) from the wall at $\tilde{z} = 0$ to the sheet at $\tilde{z} = \tilde{h}$, and applying Leibniz integral rule together with the kinematic boundary condition $\partial h/\partial t + \boldsymbol{v}_\perp \boldsymbol{\nabla}_\perp h = v_z|_{z=h}$ yields

$$\frac{\partial h}{\partial t} + \boldsymbol{\nabla}_\perp \cdot \boldsymbol{q} = 0, \tag{A 5}$$

with $\boldsymbol{q} = \int_0^h \boldsymbol{v}_\perp \,\mathrm{d}z = \tilde{\boldsymbol{q}}/\tilde{\omega}\tilde{L}\tilde{h}$ the volumetric flux along the wall.

We then follow ideas from Rojas *et al.* (2010), who included the effects of inertia at first order in the Reynolds number to study thin liquid films: we adapt their derivation to consider a solid surface instead. We start with a Taylor expansion of the velocity and pressure in the normal direction:

$$\begin{aligned}
\boldsymbol{v}_\perp(\boldsymbol{x}, t) &= \sum_{n=0}^{+\infty} \boldsymbol{v}_n(\boldsymbol{x}_\perp, t)\frac{z^{n+1}}{(n+1)!},\\
v_z(\boldsymbol{x}, t) &= -\sum_{n=0}^{+\infty} \left(\boldsymbol{\nabla}_\perp \cdot \boldsymbol{v}_n\right)(\boldsymbol{x}_\perp, t)\frac{z^{n+2}}{(n+2)!},\\
p(\boldsymbol{x}, t) &= \sum_{n=0}^{+\infty} p_n(\boldsymbol{x}_\perp, t)\frac{z^n}{n!}.
\end{aligned} \tag{A 6}$$

We can write the first expression thanks to the no-slip condition $\boldsymbol{v}_\perp = 0$ at $z = 0$, while the second expression comes from both the no-penetration condition $v_z = 0$ at $z = 0$ and the continuity equation (A 4*c*). Inserting (A 6) into (A 4) and identifying the coefficients of the Taylor series yields:

$$\begin{aligned}
p_{n\geqslant 1} &= \mathcal{O}(\varepsilon^2, \varepsilon^2 \mathrm{R_e}),\\
\boldsymbol{v}_1 &= \boldsymbol{\nabla}_\perp p_0,\\
\boldsymbol{v}_2 &= \mathrm{R_e}\frac{\partial \boldsymbol{v}_0}{\partial t} + \mathcal{O}(\varepsilon^2),\\
\boldsymbol{v}_3 &= \mathrm{R_e}\left[\frac{\partial\left(\boldsymbol{\nabla}_\perp p_0\right)}{\partial t} + 2\left(\boldsymbol{v}_0\cdot\boldsymbol{\nabla}_\perp\right)\boldsymbol{v}_0 - \boldsymbol{v}_0\left(\boldsymbol{\nabla}_\perp\cdot\boldsymbol{v}_0\right)\right] + \mathcal{O}(\varepsilon^2),\\
\boldsymbol{v}_4 &= \mathrm{R_e}\left[3\left(\boldsymbol{\nabla}_\perp p_0\cdot\boldsymbol{\nabla}_\perp\right)\boldsymbol{v}_0 - 3\left(\boldsymbol{\nabla}_\perp\cdot\boldsymbol{v}_0\right)\boldsymbol{\nabla}_\perp p_0 + 3\left(\boldsymbol{v}_0\cdot\boldsymbol{\nabla}_\perp\right)\boldsymbol{\nabla}_\perp p_0 - \right.\\
&\qquad \left. -\boldsymbol{v}_0\left(\boldsymbol{\nabla}_\perp^2 p_0\right)\right] + \mathcal{O}\left(\varepsilon^2, \varepsilon^2\mathrm{R_e}, {\mathrm{R_e}}^2\right),\\
\boldsymbol{v}_5 &= \mathrm{R_e}\left[-4\boldsymbol{\nabla}_\perp p_0\left(\boldsymbol{\nabla}_\perp^2 p_0\right) + 6\left(\boldsymbol{\nabla}_\perp p_0\cdot\boldsymbol{\nabla}_\perp\right)\boldsymbol{\nabla}_\perp p_0\right] + \mathcal{O}\left(\varepsilon^2, \varepsilon^2\mathrm{R_e}, {\mathrm{R_e}}^2\right),\\
\boldsymbol{v}_{n\geqslant 6} &= \mathcal{O}\left(\varepsilon^2, \varepsilon^2\mathrm{R_e}, {\mathrm{R_e}}^2\right).
\end{aligned} \tag{A 7}$$

We seek $\boldsymbol{v}_0$ and p_0 and expand them in powers of the Reynolds number:

$$\begin{aligned} \boldsymbol{v}_0 &= \boldsymbol{v}_0^{(0)} + \mathrm{R_e}\, \boldsymbol{v}_0^{(1)} + \mathcal{O}(\mathrm{R_e}^2), \\ p_0 &= p_0^{(0)} + \mathrm{R_e}\, p_0^{(1)} + \mathcal{O}(\mathrm{R_e}^2). \end{aligned} \tag{A 8}$$

Using the definition of the volumetric flux $\boldsymbol{q}$ and evaluating the no-slip condition $\boldsymbol{v}_\perp = 0$ at $z = h$, we find:

$$\begin{aligned} \boldsymbol{q} = &\left[\boldsymbol{v}_0^{(0)}\frac{h^2}{2!} + \boldsymbol{\nabla}_\perp p_0^{(0)}\frac{h^3}{3!}\right] + \\ &\mathrm{R_e}\left[\boldsymbol{v}_0^{(1)}\frac{h^2}{2!} + \boldsymbol{\nabla}_\perp p_0^{(1)}\frac{h^3}{3!} + \boldsymbol{v}_2^{(1)}\frac{h^4}{4!} + \boldsymbol{v}_3^{(1)}\frac{h^5}{5!} + \boldsymbol{v}_4^{(1)}\frac{h^6}{6!} + \boldsymbol{v}_5^{(1)}\frac{h^7}{7!}\right], \\ 0 = &\left[\boldsymbol{v}_0^{(0)} h + \boldsymbol{\nabla}_\perp p_0^{(0)}\frac{h^2}{2!}\right] + \\ &\mathrm{R_e}\left[\boldsymbol{v}_0^{(1)} h + \boldsymbol{\nabla}_\perp p_0^{(1)}\frac{h^2}{2!} + \boldsymbol{v}_2^{(1)}\frac{h^3}{3!} + \boldsymbol{v}_3^{(1)}\frac{h^4}{4!} + \boldsymbol{v}_4^{(1)}\frac{h^5}{5!} + \boldsymbol{v}_5^{(1)}\frac{h^6}{6!}\right]. \end{aligned} \tag{A 9}$$

We can solve this linear system order by order to express $\boldsymbol{v}_0$ and $\boldsymbol{\nabla}_\perp p_0$ as a function of $\boldsymbol{q}$ and h:

$$\begin{aligned} \boldsymbol{v}_0^{(0)} &= \frac{6\boldsymbol{q}}{h^2}, \\ \boldsymbol{\nabla}_\perp p_0^{(0)} &= -\frac{12\boldsymbol{q}}{h^3}, \\ \boldsymbol{v}_0^{(1)} &= \frac{h^2}{12}\boldsymbol{v}_2^{(1)} + \frac{h^3}{30}\boldsymbol{v}_3^{(1)} + \frac{h^4}{120}\boldsymbol{v}_4^{(1)} + \frac{h^5}{630}\boldsymbol{v}_5^{(1)}, \\ \boldsymbol{\nabla}_\perp p_0^{(1)} &= -\frac{h}{2}\boldsymbol{v}_2^{(1)} - \frac{3h^2}{20}\boldsymbol{v}_3^{(1)} - \frac{h^3}{30}\boldsymbol{v}_4^{(1)} - \frac{h^4}{168}\boldsymbol{v}_5^{(1)}, \end{aligned} \tag{A 10}$$

where the v_n, $n \geqslant 2$, are found from (A 7). After lengthy calculations, we find the contribution at $\mathcal{O}(\mathrm{R_e})$ of the pressure gradient as:

$$\boldsymbol{\nabla}_\perp p_0^{(1)} = -\frac{6}{5}\frac{\partial}{\partial t}\left(\frac{\boldsymbol{q}}{h}\right) - \frac{54}{35}\frac{\boldsymbol{q}}{h}\cdot\boldsymbol{\nabla}_\perp\left(\frac{\boldsymbol{q}}{h}\right) + \frac{6}{35}\frac{\boldsymbol{q}}{h^2}\frac{\partial h}{\partial t}, \tag{A 11}$$

which is the same as for the case of a free surface (Rojas *et al.* 2010), even though the velocity profile (A 7) differs. Equation (A 10) finally gives the link between the velocity flux $\boldsymbol{q}$ flux and the pressure gradient as:

$$12\boldsymbol{q} + h^3\boldsymbol{\nabla}_\perp p + \frac{6}{5}\mathrm{R_e}h^3\left(\frac{\partial}{\partial t}\left(\frac{\boldsymbol{q}}{h}\right) + \frac{9}{7}\frac{\boldsymbol{q}}{h}\cdot\boldsymbol{\nabla}_\perp\left(\frac{\boldsymbol{q}}{h}\right) - \frac{1}{7}\frac{\boldsymbol{q}}{h^2}\frac{\partial h}{\partial t}\right) = 0, \tag{A 12a}$$

or, in dimensional units:

$$12\tilde{\mu}\tilde{\boldsymbol{q}} + \tilde{h}^3\tilde{\boldsymbol{\nabla}}_\perp\tilde{p} + \frac{6}{5}\tilde{\rho}\tilde{h}^3\left(\frac{\partial}{\partial\tilde{t}}\left(\frac{\tilde{\boldsymbol{q}}}{\tilde{h}}\right) + \frac{9}{7}\frac{\tilde{\boldsymbol{q}}}{\tilde{h}}\cdot\boldsymbol{\nabla}_\perp\left(\frac{\tilde{\boldsymbol{q}}}{\tilde{h}}\right) - \frac{1}{7}\frac{\tilde{\boldsymbol{q}}}{\tilde{h}^2}\frac{\partial\tilde{h}}{\partial\tilde{t}}\right) = 0. \tag{A 12b}$$

This recovers the results of the analyses of Kuzma (1968); Tichy & Winer (1970); Jones & Wilson (1975) when h is the distance between two rigid, horizontal plates with then $h = h(t)$, $q(x,t) = -(x/h)\mathrm{d}h/\mathrm{d}t$ in 1D and $q(r,t) = -(r^2/2h)\mathrm{d}h/\mathrm{d}t$ in axisymmetric cylindrical coordinates with r the radial coordinate. This also matches the first-order correction of Ishizawa (1966) when, in addition, $h(t)$ oscillates

sinusoidally. We note that in (A 12), the terms in parenthesis come respectively from the terms $\partial \boldsymbol{u}_\perp/\partial t$, $\boldsymbol{u}_\perp \cdot \boldsymbol{\nabla} \boldsymbol{u}_\perp$ and $\tilde{u}_z \partial \boldsymbol{u}_\perp/\partial z$ of the horizontal momentum balance (A 4*a*), with $\boldsymbol{q}/h$ is the averaged horizontal velocity in the gap and $(1/h)\partial h/\partial t$ the average vertical gradient of vertical velocity.

Appendix B. Pressure boundary condition

Without fluid inertia, for $\mathrm{Re}_{\mathrm{bv}} = 0$, we can impose the pressure at the edge of the sheet to match the ambient pressure: $p = 0$. There is, in fact, a non-slender region near the edges connecting the gap to the outside where lubrication theory might break down. There, we assume that the pressure difference scales as $\Delta\tilde{p} \sim \tilde{\mu}\tilde{v}_\perp/\tilde{L} \sim \tilde{\mu}\tilde{\omega}$ with $\tilde{v}_\perp = \tilde{\omega}\tilde{L}$ the horizontal velocity scale. Comparing this to the dynamic pressure that scales as, we find $\tilde{\rho}_a(\tilde{\omega}\tilde{H}_{\mathrm{bv}})^2/\Delta\tilde{p} \sim \mathrm{Re}_{\mathrm{bv}}$, which suggests a boundary effect at $\mathcal{O}(\mathrm{Re}_{\mathrm{bv}})$.

This problem has been discussed in prior works. For the steady translation of a rigid sheet, Tuck & Bentwich (1983) argue that when fluid leaves the gap, the pressure at the edge matches the ambient pressure. This is a classical condition for a jet. However, when fluid enters the gap, the entrance flow is not jet-like, and fluid is drawn from an extended region, leading to a pressure drop. Significant effects of inertia on the pressure distribution can arise due to this sole asymmetry in entrance and exit boundary conditions (Tuck & Bentwich 1983; Tichy & Bourgin 1985). For thin film flows between an oscillating plate and a stationary wall, the early study of Kuroda & Hori (1976) has been extensively followed (Hori 2006) and matches the work of Tuck & Bentwich (1983): at the edges, the author assumes $p = 0$ when $\boldsymbol{q} \cdot \boldsymbol{e_r} > 0$ (outflow) and $\tilde{p} = -(k/2)\tilde{\rho}_a(\tilde{\boldsymbol{q}} \cdot \boldsymbol{e_r}/\tilde{h})^2$ otherwise (inflow). Here, $\tilde{\boldsymbol{q}} \cdot \boldsymbol{e_r}/\tilde{h}$ is the average velocity of the fluid leaving or entering the gap, and $k > 0$ is a dimensionless coefficient taking into account losses in the Bernoulli pressure drop. In dimensionless quantities, this boundary condition reads:

$$p = \begin{cases} 0 & \text{if } \boldsymbol{q} \cdot \boldsymbol{e}_r > 0 \quad \text{(outflow)} \\ -\dfrac{k}{2}\mathrm{Re}_{\mathrm{bv}} \left(\dfrac{\boldsymbol{q} \cdot \boldsymbol{e}_r}{h}\right)^2 & \text{if } \boldsymbol{q} \cdot \boldsymbol{e}_r < 0 \quad \text{(inflow)} \end{cases} . \tag{B 1}$$

The value $k = 0.5$ is often adopted (Kuroda & Hori 1976; Hori 2006) by analogy with high-Reynolds-number pipe flows (Çengel & Cimbala 2013).

Recently, Ramanarayanan *et al.* (2022) studied in detail the effect of inertia for the flow under a flat and circular rigid plate undergoing oscillations above a solid substrate as $\tilde{h}(\tilde{t}) = \tilde{h}_0(1 + a\sin(\tilde{\omega}\tilde{t}))$, $0 < a < 1$. They matched the thin film flow in the gap to solutions of the Navier-Stokes equations outside the gap for a wide range of Reynolds numbers $\mathrm{R_e} = \tilde{\rho}_a\tilde{\omega}\tilde{h}_0/\tilde{\mu}$. They found that the pressure at the edges averaged over one period of oscillation is $\langle\tilde{p}_e\rangle = -K\tilde{\rho}_a\tilde{R}^2a^2\tilde{\omega}^2$, with K a coefficient found numerically. For $\mathrm{R_e} \lesssim 5$, $K \approx 0.096$. For $\mathrm{R_e} \gtrsim 100$, $K = 1/16$ if $(\tilde{H}/\tilde{R}) \ll a$, $K = 1/32$ if $(\tilde{H}/\tilde{R}) \gg a$. The boundary condition (B 1) applied to the same situation yields the same scaling: $\langle\tilde{p}_e\rangle = -(k\pi/16)\tilde{\rho}\tilde{L}^2a^2\tilde{\omega}^2$. This matches the various cases studied by Ramanarayanan *et al.* (2022) if $k \simeq 0.49$, $k \simeq 0.32$ and $k \simeq 0.16$, respectively. Since we will be dealing with Reynolds numbers that remain small, $\mathrm{R_e} < 10$, we adopt (B 1) with $k = 0.5$.

Appendix C. Viscous adhesion under weak active forcing

To study theoretically (3.1) with the force balance (2.6), we use a Galerkin projection of the height. We let

$$h(x,t) = h_0(t) + \mathcal{G}H_1(x) + \alpha\cos(t)H_0(x) + \alpha\sum_{i=1}^{\infty} a_i(t)\zeta_i(x), \tag{C 1a}$$

where $h_0(t)$ and $(a_i(t))_{i\in\mathbb{N}^\star}$ are unknown time-dependent coefficients. The functions H_0, H_1 and $(\zeta_i)_{i\in\mathbb{N}^\star}$ are chosen as:

$$H_0(x) = -\frac{x^6}{240} + \frac{x^4}{16} - \frac{|x|^3}{6} + \frac{3x^2}{16}, \quad H_1(x) = -\frac{x^6}{240} + \frac{x^4}{48} - \frac{x^2}{16}, \tag{C 1b}$$

$$\zeta_n(x) = I_n \times \begin{cases} (-1)^{\frac{n}{2}}\cosh\left(\frac{\sqrt{3}}{2}n\pi\right)\cos(n\pi x) + 2\cosh\left(n\pi\frac{\sqrt{3}}{2}x\right)\cos\left(\frac{n\pi}{2}x\right), & n \text{ even} \\ (-1)^{\frac{n-1}{2}}\sinh\left(\frac{\sqrt{3}}{2}n\pi\right)\cos(n\pi x) - 2\sinh\left(n\pi\frac{\sqrt{3}}{2}x\right)\sin\left(\frac{n\pi}{2}x\right), & n \text{ odd}, \end{cases}$$

with I_n a normalization coefficient ensuring that $\int_0^1 \zeta_n^2 = 1$. This expansion matches the first-order deformation H_1 and H_0 due to a uniform load and to a point-active forcing, respectively, while allowing for higher-order modes of deformation. The ζ_n, shown in figure 2(*d*), are the even eigenmodes of the triharmonic operator $\partial/\partial x^6$ satisfying the boundary conditions $\partial^2\zeta_n/\partial x^2 = \partial^3\zeta_n/\partial x^3 = \partial^4\zeta_n/\partial x^4 = 0$ at $x = \pm 1$, such that this ansatz for h satisfies the boundary conditions (2.10) and (2.11).

Upon inserting (C 1) in the governing equations and projecting in space, we make use of an averaging method considering a separation of timescales between the fast oscillation time t and the slow time $\alpha^2 t$ associated with the long-time evolution of the system (figure 1*b*). This gives rise to an evolution equation at $\mathcal{O}(\alpha^2)$ for $\langle h_0\rangle(t) = \int_t^{t+2\pi} h(x=0,t')\,\mathrm{d}t'$, the time-averaged evolution of the sheet's centre height, given by (3.2).

Up to $N = 5$, the coefficients d_{ij} appearing in (3.2) are found numerically and are given by the entries of the following symmetric matrix

$$\mathbf{d} = \begin{pmatrix} 1.14\times10^{-2} & 2.04\times10^{-6} & -6.91\times10^{-6} & 1.64\times10^{-5} & -3.24\times10^{-5} \\ & 6.95\times10^{-4} & 9.24\times10^{-7} & -2.05\times10^{-6} & 4.01\times10^{-6} \\ & & 1.49\times10^{-4} & 7.08\times10^{-7} & -1.24\times10^{-6} \\ & & & 3.00\times10^{-5} & 6.12\times10^{-7} \\ & & & & 4.73\times10^{-5} \end{pmatrix}, \tag{C 2}$$

and $d_0 = 0.122$.

Appendix D. Rigid sheet and non-zero Reynolds number

We consider the case of a rigid and weightless 1-dimensional sheet in an incompressible fluid to isolate the effects of fluid inertia: $\tilde{B}\to\infty$, $\mathcal{G} = 0$, $\mathrm{S_q} = 0$, $\mathrm{R_e} > 0$. The governing equations reduce to:

$$12\frac{\partial h}{\partial t} - \frac{\partial}{\partial x}\left(h^3\frac{\partial p}{\partial x}\right) = 0, \tag{D 1a}$$

$$\int_{-1}^{+1} p\,\mathrm{d}x = -2\alpha\cos(t), \tag{D 1b}$$

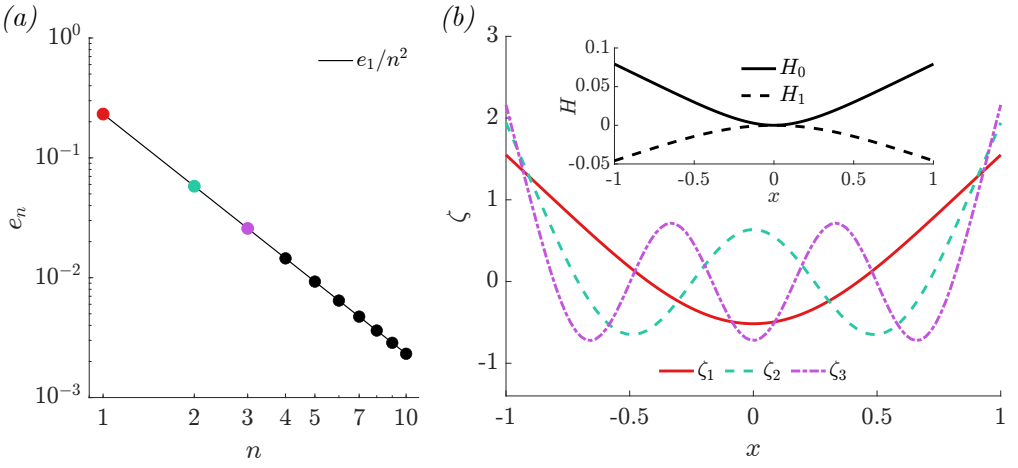

Figure 11: Asymptotic results for $\alpha \lesssim 1$, $\mathcal{I}_{\rm bv} = {\rm Re}_{\rm bv} = {\rm Sq}_{\rm bv} = 0$, adapted from Poulain *et al.* (2025). As $\mathcal{G}$ and $h_{\rm eq}$ decrease, the sheet presents higher and higher order deformation modes. The $i-$th mode ζ_i is excited if $h \lesssim e_i$.

with the boundary condition at $x = \pm 1$:

$$p = \begin{cases} 0 & \text{if } q > 0 \\ -\dfrac{k}{2}{\rm R_e}\left(\dfrac{q}{h}\right)^2 & \text{if } q < 0 \end{cases}. \tag{D 1c}$$

We consider a sheet aligned with the wall, $h = h(t)$. We can express the pressure gradient as a function of the height h from (D 1):

$$\frac{1}{x}\frac{\partial p}{\partial x} = 12\frac{\dot{h}}{h^3} + \frac{6{\rm R_e}}{5}\frac{\ddot{h}}{h} - \frac{102{\rm R_e}}{35}\frac{\dot{h}^2}{h^2}. \tag{D 2}$$

This can directly be integrated using the boundary condition to give the pressure profile in the gap:

$$p(x,t) = \left(1 - x^2\right)\left(-6\frac{\dot{h}}{h^3} - \frac{3{\rm R_e}}{5}\frac{\ddot{h}}{h} + \frac{51{\rm R_e}}{35}\frac{\dot{h}^2}{h^2}\right) + p_{\rm edge}, \tag{D 3}$$

$$p_{\rm edge} = -\frac{k}{2}{\rm R_e}\mathbb{H}\left(\dot{h}\right)\left(\frac{\dot{h}}{h}\right)^2, \tag{D 4}$$

with $\mathbb{H}$ the Heaviside function. Using (D 1*b*), this leads to the following ordinary differential equation for $h(t)$, together with the initial conditions $h(0) = 1,\ \dot{h}(0) = 0$:

$$\frac{2{\rm R_e}}{5h}\ddot{h} + 4\frac{\dot{h}}{h^3} + {\rm R_e}\frac{\dot{h}^2}{h^2}\left[\frac{k}{2}\mathbb{H}\left(\dot{h}\right) - \frac{34}{35}\right] - \alpha\cos(t) = 0. \tag{D 5}$$

We note that the unsteady inertial term, proportional to $\ddot{h}$, appears as an added mass as mentioned in §4.1.

To find an approximate solution to (D 5), we introduce a slow timescale $\tau_{\rm Re} = {\rm R_e}t$ and expand the height in powers of the Reynolds number:

$$h(t) = h_0(t, \tau_{\rm Re}) + {\rm R_e}h_1(t, \tau_{\rm Re}) + \mathcal{O}({\rm R_e}^2). \tag{D 6}$$

Inserting into (D 5) yields:

$$\mathcal{O}(1): \quad 4\frac{\partial h_0}{\partial t} + \alpha\cos(t)h_0^3 = 0, \tag{D 7a}$$

$$\mathcal{O}(\mathrm{R_e}): \quad 4\frac{\partial h_1}{\partial t} + 3h_0^2\alpha\cos(t)h_1 = -4\frac{\partial h_0}{\partial \tau_{\mathrm{Re}}} - \frac{2}{5}h_0^2\frac{\partial^2 h_0}{\partial t^2} + h_0\left(\frac{\partial h_0}{\partial t}\right)^2\left[\frac{34}{35} - \frac{k}{2}\mathbb{H}\left(\dot{h}_0\right)\right]. \tag{D 7b}$$

Equation (D 7*a*) can be integrated directly as a linear differential equation in t. Introducing $f_{\mathrm{R_e}}(\tau_{\mathrm{R_e}})$ as an integration constant (a function of $\tau_{\mathrm{R_e}}$ independent of t), we find:

$$h_0 = \left[f_{\mathrm{Re}}(\tau_{\mathrm{Re}}) + \frac{\alpha}{2}\sin(t)\right]^{-1/2}. \tag{D 8}$$

Knowing h_0, (D 7*b*) is also a linear ordinary differential equation for h_1 which can be solved as:

$$h_1(t,\tau_{\mathrm{Re}}) = h_0^3(t)\int_0^t\left[-\frac{1}{h_0^3}\frac{\partial h_0}{\partial \tau_{\mathrm{Re}}} - \frac{1}{10h_0}\frac{\partial^2 h_0}{\partial t^2} + \frac{1}{h_0^2}\left(\frac{\partial h_0}{\partial t}\right)^2\left(\frac{17}{70} - \frac{k}{8}\mathbb{H}\left(\frac{\partial h_0}{\partial t}\right)\right)\right]\mathrm{d}t'. \tag{D 9}$$

Both h_0 and the integrand of (D 9) are $2\pi-$periodic in t. Therefore, if the average value of the integrand was non-zero, $h_1(t)$ would diverge as $t\to\infty$. This would break the asymptotic expansion (D 6). We conclude that this integrand must have a zero mean, which is equivalent to requesting that h_1 must be 2π-periodic in t. In particular, $h_1(0,\tau_{\mathrm{Re}}) = h_1(2\pi,\tau_{\mathrm{Re}})$. This non-secularity condition gives a differential equation for $f_{\mathrm{Re}}(\tau_{\mathrm{Re}})$:

$$\pi f'_{\mathrm{Re}}(\tau_{\mathrm{Re}}) = \frac{\alpha}{40}\int_0^{2\pi}\frac{\sin(t)}{f_{\mathrm{Re}}(\tau_{\mathrm{Re}}) + \frac{\alpha}{2}\cos(t)}\mathrm{d}t + \frac{\alpha^2}{280}\int_0^{2\pi}\frac{\cos^2(t)}{\left(f_{\mathrm{Re}}(\tau_{\mathrm{Re}}) + \frac{\alpha}{2}\sin(t)\right)^2}\mathrm{d}t + \frac{k\alpha^2}{128}\int_{\pi/2}^{3\pi/2}\frac{\cos^2(t)}{\left(f_{\mathrm{Re}}(\tau_{\mathrm{Re}}) + \frac{\alpha}{2}\sin(t)\right)^2}\mathrm{d}t. \tag{D 10}$$

We approximate the integrals using a first-order Taylor expansion for small $\Gamma/2f_{\mathrm{Re}}$ and find:

$$f_{\mathrm{Re}}^2(\tau_{\mathrm{R_e}})f'_{\mathrm{Re}}(\tau_{\mathrm{R_e}}) = -\frac{1}{112}\left(1 - \frac{7k}{16}\right)\alpha^2,$$

$$f_{\mathrm{Re}}(\tau_{\mathrm{Re}}) = \left(1 - \frac{3}{112}\left(1 - \frac{7k}{16}\right)\alpha^2\tau_{\mathrm{Re}}\right)^{1/3}, \tag{D 11}$$

$$h_0(t) = \left[\left(1 - \frac{3}{112}\left(1 - \frac{7k}{16}\right)\alpha^2\mathrm{R_e}t\right)^{1/3} + \frac{\alpha}{2}\sin(t)\right]^{-1/2}.$$

We have kept an arbitrary value for the loss coefficient k for completeness. We argue in Appendix B for $k = 0.5$, and with this value $3(1-7k/16)/112 \simeq 0.021$. Therefore,

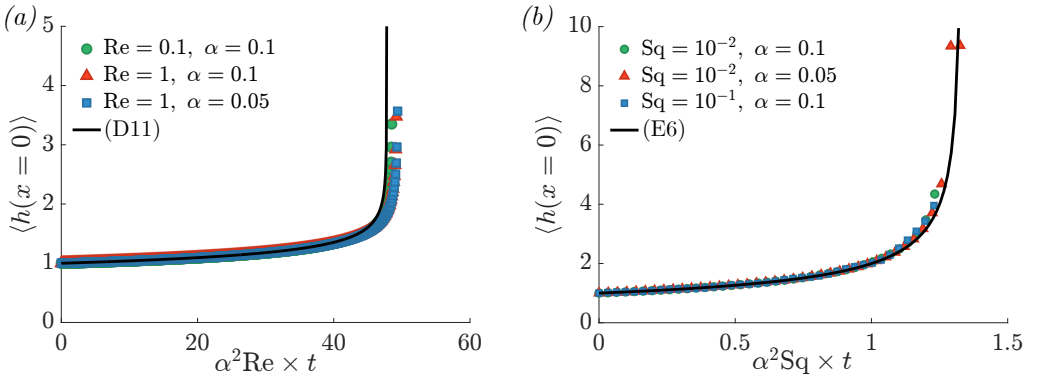

Figure 12: Comparison between numerical results (symbols) and first-order asymptotic calculations from two-timescale analysis (lines) for the height evolution of a rigid sheet with (*a*) $\mathrm{Re} > 0$, $\mathrm{Sq} = 0$ and (*b*) $\mathrm{Sq} > 0$, $\mathrm{Re} = 0$.

$\langle h \rangle(t) \simeq \left(1 - 0.021\alpha^2 \mathrm{R_e} t\right)^{-1/6}$, where we denote $\langle h \rangle(t) = \int_{t'}^{t'+2\pi} h(t')\mathrm{d}t'/2\pi$ the time-averaged evolution. These results are verified in figure 12(*a*).

Appendix E. Rigid sheet and non-zero Squeeze number

We neglect inertia, $\mathrm{R_e} = 0$, but assume a non-zero squeeze number $\mathrm{S_q} > 0$. The mass conservation equation (2.4) and the momentum balance (2.5) give:

$$12\frac{\partial(\rho h)}{\partial t} - \frac{\partial}{\partial x}\left(\rho h^3 \frac{\partial p}{\partial x}\right) = 0, \quad \rho = 1 + \mathrm{S_q} p. \tag{E 1}$$

We let $\tau_{\mathrm{Sq}} = \mathrm{S_q} t$ and expand $h(t) = h_0(t, \tau_{\mathrm{Sq}}) + \mathrm{S_q} h_1(t, \tau_{\mathrm{Sq}}) + \mathcal{O}(\mathrm{S_q^2})$ and $p(x,t) = p_0(x,t,\tau_{\mathrm{Sq}}) + \mathrm{S_q} p_1(x,t,\tau_{\mathrm{Sq}}) + \mathcal{O}(\mathrm{S_q^2})$. Collecting terms of the same order, (E 1) yields

$$\mathcal{O}(1): \quad 12\frac{\partial h_0}{\partial t} - h_0^3 \frac{\partial^2 p_0}{\partial x^2} = 0, \tag{E 2a}$$

$$\mathcal{O}(\mathrm{S_q}): \quad 12\frac{\partial h_1}{\partial t} - h_0^3 \frac{\partial^2 p_1}{\partial x^2} = - 12\frac{\partial (p_0 h_0)}{\partial t} - 12\frac{\partial h_0}{\partial \tau_{\mathrm{Sq}}} + 3h_0^2 h_1 \frac{\partial^2 p_0}{\partial x^2} + h_0^3 \frac{\partial}{\partial x}\left(p_0 \frac{\partial p_0}{\partial x}\right), \tag{E 2b}$$

while the integrated version of the force balance (2.6) and the boundary condition (2.11) yield

$$\int_{-1}^{1} p_0 \, \mathrm{d}x = 2\alpha\cos(t), \quad \int_{-1}^{+1} p_1 \, \mathrm{d}x = 0, \quad p_0(x = \pm 1, t) = p_1(x = \pm 1, t) = 0. \tag{E 3}$$

The problem at $\mathcal{O}(1)$ is simply the rigid incompressible problem, and the solution is directly found as

$$p_0 = \frac{\alpha}{4}\cos(t)(1 - x^2), \quad h_0 = \left(f_{\mathrm{Sq}}(\tau_{\mathrm{Sq}}) + \frac{\alpha}{2}\sin(t)\right)^{-1/2}, \tag{E 4}$$

with $f_{\mathrm{Sq}}(\tau_{\mathrm{Sq}})$ an integration constant that depends on the slow time. At $\mathcal{O}(\mathrm{S_q})$ we can

integrate (E 2*b*) to obtain p_1, then use the force balance to obtain a single ordinary differential equation for h_1:

$$\frac{\partial h_1}{\partial t} + \frac{3\alpha\cos(t)}{4\,(1+\alpha\sin(t)/2)}h_1 = \frac{20 f'_{\mathrm{Sq}}(\tau_{\mathrm{Sq}}) + 30\alpha^2 - 18\alpha^2\cos(2t) + 96\alpha f_{\mathrm{Sq}}(\tau_{\mathrm{Sq}})\sin(t)}{80\,(1+\alpha\sin(t)/2)^{3/2}}. \tag{E 5}$$

Using a non-secularity condition similar to the one used in appendix D, we find:

$$f'_{\mathrm{Sq}}(\tau_{\mathrm{Sq}}) = -\frac{3\alpha^2}{4}, \quad f_{\mathrm{Sq}}(\tau_{\mathrm{Sq}}) = 1 - \frac{3\alpha^2}{4}\tau_{\mathrm{Sq}}, \quad h_0(t) \approx \left(1 - \frac{3}{4}\alpha^2 \mathrm{S_q} t\right)^{-1/2}, \tag{E 6}$$

which is verified in figure 12(*b*). The pressure at $\mathcal{O}(\mathrm{S_q})$ is

$$p_1(x,t,\tau) = \frac{3\alpha}{20}\left(1-x^2\right)\left(5x^2-1\right)\left[\alpha\cos(2t) - 2f_{\mathrm{Sq}}(\tau_{\mathrm{Sq}})\sin(t)\right]. \tag{E 7}$$

REFERENCES

Alexander, R. 1977 Diagonally implicit Runge-Kutta methods for stiff O.D.E.'s. *SIAM Journal on Numerical Analysis* **14** (6), 1006–1021.

Andrade, M.A.B., Pérez, N. & Adamowski, J.C. 2018 Review of progress in acoustic levitation. *Braz. J. Phys.* **48**, 190–213.

Andrade, M.A.B., Ramos, T.S., Adamowski, J.C. & Marzo, A. 2020 Contactless pick-and-place of millimetric objects using inverted near-field acoustic levitation. *Appl. Phys. Lett.* **116** (5).

Argentina, M., Skotheim, J. & Mahadevan, L. 2007 Settling and swimming of flexible fluid-lubricated foils. *Phys. Rev. Lett.* **99** (22), 224503.

Atalla, M.A., Van Ostayen, R.A.J., Sakes, A. & Wiertlewski, M. 2023 Incompressible squeeze-film levitation. *Appl. Phys. Lett.* **122** (24).

Bao, M. & Yang, H. 2007 Squeeze film air damping in MEMS. *Sens. Actuator A-Phys.* **136** (1), 3–27.

Batchelor, G.K. 1967 *An Introduction to Fluid Dynamics*. Cambridge University Press.

Bertin, V., Oratis, A. & Snoeijer, J.H. 2025 Sticking without contact: elastohydrodynamic adhesion. *Phys. Rev. X* **15** (2), 021006.

Bhosale, Y., Parthasarathy, T. & Gazzola, M. 2022 Soft streaming–flow rectification via elastic boundaries. *J. Fluid Mech.* **945**, R1.

Bigan, N., Lizée, M., Pascual, M., Niguès, A., Bocquet, L. & Siria, A. 2024 Long range signature of liquid's inertia in nanoscale drainage flows. *Soft Matter* **20** (44), 8804–8811.

Brennen, C.E. 1982 A review of added mass and fluid inertial forces. *Tech. Rep. CR 82.010* Naval Civil Engineering Laboratory.

Bureau, L., Coupier, G. & Salez, T. 2023 Lift at low Reynolds number. *Eur. Phys. J. E* **46** (11), 111.

Calisti, M., Picardi, G. & Laschi, C. 2017 Fundamentals of soft robot locomotion. *J. R. Soc. Interface.* **14** (130), 20170101.

Colasante, D.A. 2015 Apparatus and method for orthosonic lift by deflection. U.S. Patent US8967965B1.

Colasante, D. 2016 Youtube videos. Available at https://www.youtube.com/watch?v=kG6vXGidQbo (2016) and https://www.youtube.com/watch?v=ruDpMhlKy6M (2024). Accessed on April 9, 2025.

Cui, S., Bhosale, Y. & Gazzola, M. 2024 Three-dimensional soft streaming. *J. Fluid Mech.* **979**, A7.

Dragon, C.A. & Grotberg, J.B. 1991 Oscillatory flow and mass transport in a flexible tube. *J. Fluid Mech.* **231**, 135–155.

Essink, M.H., Pandey, A., Karpitschka, S., Venner, C.H. & Snoeijer, J.H. 2021 Regimes of soft lubrication. *J. Fluid Mech.* **915**, A49.

Fedder, G.K., Hierold, C., Korvink, J.G. & Tabata, O. 2015 *Resonant MEMS: fundamentals, implementation, and application*. John Wiley & Sons.

Fouxon, I. & Leshansky, A. 2018 Fundamental solution of unsteady Stokes equations and force on an oscillating sphere near a wall. *Phys. Rev. E* **98** (6), 063108.

Fouxon, I., Rubinstein, B., Weinstein, O. & Leshansky, A. 2020 Fluid-mediated force on a particle due to an oscillating plate and its effect on deposition measurements by a quartz crystal microbalance. *Phys. Rev. Lett.* **125** (14), 144501.

Glowinski, R., Pan, T.-W., Hesla, T.I., Joseph, D.D. & Periaux, J. 2001 A fictitious domain approach to the direct numerical simulation of incompressible viscous flow past moving rigid bodies: application to particulate flow. *J. Comput. Phys.* **169** (2), 363–426.

Hall, P. 1974 Unsteady viscous flow in a pipe of slowly varying cross-section. *J. Fluid Mech.* **64** (2), 209–226.

Hashimoto, Y., Koike, Y. & Ueha, S. 1996 Near-field acoustic levitation of planar specimens using flexural vibration. *J. Acoust. Soc. Am.* **100** (4), 2057–2061.

Haynes, W.M. 2016 *CRC handbook of chemistry and physics*. CRC press.

Hori, Y. 2006 *Hydrodynamic lubrication*. Springer.

Ishizawa, S. 1966 The unsteady laminar flow between two parallel discs with arbitrarily varying gap width. *Bulletin of JSME* **9** (35), 533–550.

Jia, C., Ramanarayanan, S., Sanchez, A.L. & Tolley, M.T. 2023 Controlling the motion of gas-lubricated adhesive disks using multiple vibration sources. *Front. Robot. AI.* **10**, 1231976.

Jones, A.F. & Wilson, S.D.R. 1975 On the failure of lubrication theory in squeezing flows. *J. Tribol.* .

Koch, T., Weishaupt, K., Gläser, D. & others 2021 DuMux 3 – an open-source simulator for solving flow and transport problems in porous media with a focus on model coupling. *Computers & Mathematics with Applications* **81**, 423–443.

Kuroda, S. & Hori, Y. 1976 A study of fluid inertia effects in a squeeze film (in japanese). *Journal of Japan Society of Lubrication Engineers* **21** (11), 740–747.

Kuzma, D.C. 1968 Fluid inertia effects in squeeze films. *Applied Scientific Research* **18**, 15–20.

Landau, L.D. & Lifshitz, E.M. 1986 *Course of Theoretical Physics vol. 7: Theory of Elasticity*. 3rd edn. Pergamon.

Langlois, W.E. 1962 Isothermal squeeze films. *Quarterly of Applied Mathematics* **20** (2), 131–150.

Lauga, E. 2007 Floppy swimming: Viscous locomotion of actuated elastica. *Phys. Rev. E* **75** (4), 041916.

Lauga, E. 2011 Life around the scallop theorem. *Soft Matter* **7** (7), 3060–3065.

Lee, J.W., Tung, R., Raman, A., Sumali, H. & Sullivan, J.P. 2009 Squeeze-film damping of flexible microcantilevers at low ambient pressures: theory and experiment. *J. Micromech. Microeng.* **19** (10), 105029.

Li, X., Li, N., Tao, G., Liu, H. & Kagawa, T. 2015 Experimental comparison of Bernoulli gripper and vortex gripper. *Int. J. Precis. Eng. Man.* **16**, 2081–2090.

Liu, Y., Zhao, Z. & Chen, W. 2023 Theoretical investigation of the levitation force generated by underwater squeeze action. *Jpn. J. Appl. Phys.* **62** (3), 034001.

Mandre, S., Mani, M. & Brenner, M.P. 2009 Precursors to splashing of liquid droplets on a solid surface. *Phys. Rev. Lett.* **102** (13), 134502.

Melikhov, I., Chivilikhin, S., Amosov, A. & Jeanson, R. 2016 Viscoacoustic model for near-field ultrasonic levitation. *Phys. Rev. E* **94** (5), 053103.

Minikes, A. & Bucher, I. 2003 Coupled dynamics of a squeeze-film levitated mass and a vibrating piezoelectric disc: numerical analysis and experimental study. *J. Sound Vib.* **263** (2), 241–268.

Moore, D.F. 1965 A review of squeeze films. *Wear* **8** (4), 245–263.

Naghdi, P. M. 1973 The theory of shells and plates. In *Linear theories of elasticity and thermoelasticity: linear and nonlinear theories of rods, plates, and shells*, pp. 425–640. Springer.

Ollila, R.G. 1980 Historical review of WIG vehicles. *J. Hydronaut.* **14** (3), 65–76.

Pande, S.D., Wang, X. & Christov, I.C. 2023 Oscillatory flows in compliant conduits at arbitrary womersley number. *Phys. Rev. Fluids* **8** (12), 124102.

Pandey, A.K. & Pratap, R. 2007 Effect of flexural modes on squeeze film damping in MEMS cantilever resonators. *J. Micromech. Microeng.* **17** (12), 2475.

Peng, G.G., Cuttle, C., MacMinn, C.W. & Pihler-Puzović, D. 2023 Axisymmetric gas–liquid displacement flow under a confined elastic slab. *Phys. Rev. Fluids* **8** (9), 094005.

Poulain, S., Carlson, A., Mandre, S. & Mahadevan, L. 2022 Elastohydrodynamics of contact in adherent sheets. *J. Fluid Mech.* **947**, A16.

Poulain, S., Koch, T., Mahadevan, L. & Carlson, A. 2025 Hovering of an actively driven fluid-lubricated foil. *Phys. Rev. Lett.* (accepted).

Pratap, R. & Roychowdhury, A. 2014 *Vibratory MEMS and Squeeze Film Effects*, pp. 319–338. New Delhi: Springer India.

Purcell, E.M. 1977 Life at low Reynolds number. *Am. J. Phys.* **45** (1), 3–11.

Rallabandi, B. 2024 Fluid-elastic interactions near contact at low Reynolds number. *Annu. Rev. Fluid Mech.* **56**, 491–519.

Ramanarayanan, S. 2024 On the emergence of attractive load-bearing forces in vibration-induced squeeze-film gas lubrication. PhD thesis, University of California, San Diego.

Ramanarayanan, S., Coenen, W. & Sánchez, A.L. 2022 Viscoacoustic squeeze-film force on a rigid disk undergoing small axial oscillations. *J. Fluid Mech.* **933**.

Ramanarayanan, S. & Sánchez, A.L. 2022 On the enhanced attractive load capacity of resonant flexural squeeze-film levitators. *AIP Advances* **12** (10).

Ramanarayanan, S. & Sánchez, A.L. 2023 Benefits of controlled inclination for contactless transport by squeeze-film levitation. *Flow* **3**, E26.

Ramanarayanan, S. & Sánchez, A.L. 2024 The role of fluid–structure coupling in the generation of an attractive squeeze-film force. *J. Fluid Mech.* **1001**, A52.

Rayner, J.M.V. 1991 On the aerodynamics of animal flight in ground effect. *Proc. Roy. Soc. B* **334** (1269), 119–128.

Rieutord, F., Bataillou, B. & Moriceau, H. 2005 Dynamics of a bonding front. *Phys. Rev. Lett.* **94** (23), 236101.

Riley, Norman 2001 Steady streaming. *Annu. Rev. Fluid Mech.* **33** (1), 43–65.

Rojas, N.O., Argentina, M., Cerda, E. & Tirapegui, E. 2010 Inertial lubrication theory. *Phys. Rev. Lett.* **104** (18), 187801.

Salbu, E.O.J. 1964 Compressible squeeze films and squeeze bearings. *J. Basic Eng.* **86** (2), 355–364.

Shao, X., Wang, Y. & Frechette, J. 2023 Out-of-contact peeling caused by elastohydrodynamic deformation during viscous adhesion. *J. Chem. Phys.* **159** (13).

Shi, M., Feng, K., Hu, J., Zhu, J. & Cui, H. 2019 Near-field acoustic levitation and applications to bearings: a critical review. *Int. J. Extreme Manuf.* **1** (3), 032002.

Shintake, J., Cacucciolo, V., Floreano, D. & Shea, H. 2018 Soft robotic grippers. *Adv. Mater.* **30** (29), 1707035.

Shui, L., Jia, L., Li, H., Guo, J., Guo, Z., Liu, Y., Liu, Z. & Chen, X. 2020 Rapid and continuous regulating adhesion strength by mechanical micro-vibration. *Nat. Commun.* **11** (1), 1583.

Skotheim, J.M. & Mahadevan, L. 2005 Soft lubrication: The elastohydrodynamics of nonconforming and conforming contacts. *Phys. Fluids* **17** (9).

Takasaki, M., Terada, D., Kato, Y., Ishino, Y. & Mizuno, T. 2010 Non-contact ultrasonic support of minute objects. *Phys. Procedia* **3** (1), 1059–1065.

Taylor, G.I. 1967 Film notes for low-Reynolds-number flows. National Committee for Fluid Mechanics Films. Available at https://web.mit.edu/hml/ncfmf.html. Accessed on June 11, 2025.

Taylor, S.G. & Saffman, P.G. 1957 Effects of compressibility at low Reynolds number. *Journal of the Aeronautical Sciences* **24** (8), 553–562.

Tichy, J.A. & Bourgin, P. 1985 The effect of inertia in lubrication flow including entrance and initial conditions. *J. Appl. Mech.* .

Tichy, J.A. & Winer, W.O. 1970 Inertial considerations in parallel circular squeeze film bearings. *J. Lubric. Tech.* .

Timoshenko, S. & Woinowsky-Krieger, S. 1959 *Theory of plates and shells*, 2nd edn. McGraw-hill New York.

Tiwari, A. & Persson, B.N.J. 2019 Physics of suction cups. *Soft matter* **15** (46), 9482–9499.

Tricarico, M., Ciavarella, M. & Papangelo, A. 2025 Enhancement of adhesion strength through microvibrations: Modeling and experiments. *J. Mech. Phys. Solids* **196**, 106020.

Tuck, E.O. & Bentwich, M. 1983 Sliding sheets: lubrication with comparable viscous and inertia forces. *J. Fluid Mech.* **135**, 51–69.

Ueha, S., Hashimoto, Y. & Koike, Y. 2000 Non-contact transportation using near-field acoustic levitation. *Ultrasonics* **38** (1-8), 26–32.

Vandaele, V., Lambert, P. & Delchambre, A. 2005 Non-contact handling in microassembly: Acoustical levitation. *Precis. Eng.* **29** (4), 491–505.

Veijola, T. 2004 Compact models for squeezed-film dampers with inertial and rarefied gas effects. *J. Micromech. Microeng.* **14** (7), 1109.

Waltham, C., Bendall, S. & Kotlicki, A. 2003 Bernoulli levitation. *Am. J. Phys.* **71** (2), 176–179.

Wei, Z., Liu, J., Zheng, X., Sun, Y. & Wei, R. 2021 Influence of squeeze film damping on quality factor in tapping mode atomic force microscope. *J. Sound Vib.* **491**, 115720.

Weston-Dawkes, W.P., Adibnazari, I., Hu, Y.-W., Everman, M., Gravish, N. & Tolley, M.T. 2021 Gas-lubricated vibration-based adhesion for robotics. *Adv. Intell. Syst.* **3** (7), 2100001.

Whitesides, G.M. 2018 Soft robotics. *Angew. Chem. Int. Ed.* **57** (16), 4258–4273.

Wiertlewski, M., Fenton Friesen, R. & Colgate, J.E. 2016 Partial squeeze film levitation modulates fingertip friction. *Proc. Natl. Acad. Sci. U.S.A.* **113** (33), 9210–9215.

Wiggins, C.H. & Goldstein, R.E. 1998 Flexive and propulsive dynamics of elastica at low Reynolds number. *Phys. Rev. Lett.* **80** (17), 3879.

Wiggins, C.H., Riveline, D., Ott, A. & Goldstein, R.E. 1998 Trapping and wiggling: elastohydrodynamics of driven microfilaments. *Biophys. J.* **74** (2), 1043–1060.

Womersley, J. R. 1955 Method for the calculation of velocity, rate of flow and viscous drag in arteries when the pressure gradient is known. *J. Physiol.* **127** (3), 553–563.

Wriggers, P. 2006 *Computational contact mechanics*, 2nd edn. Springer.

Wu, C., Cai, A., Li, X., Gao, X. & Cao, C. 2023 A self-loading suction cup driven by a resonant dielectric elastomer actuator. *Smart Mater. Struct.* **32** (10), 105011.

Yu, T.S., Lauga, E. & Hosoi, A.E. 2006 Experimental investigations of elastic tail propulsion at low reynolds number. *Phys. Fluids* **18** (9).

Zhang, X. & Rallabandi, B. 2024 Elasto-inertial rectification of oscillatory flow in an elastic tube. *J. Fluid Mech.* **996**, A16.

Zhang, Z., Bertin, V., Essink, M.H., Zhang, H., Fares, N., Shen, Z., Bickel, T., Salez, T. & Maali, A. 2023 Unsteady drag force on an immersed sphere oscillating near a wall. *J. Fluid Mech.* **977**, A21.

Zhu, T., Liu, R., Wang, X. D. & Wang, K. 2006 Principle and application of vibrating suction method. In *2006 IEEE International Conference on Robotics and Biomimetics*, pp. 491–495. IEEE.

Çengel, Y. & Cimbala, J. 2013 *Fluid Mechanics*. McGraw Hill.